biomedicines

MDPI

Review

Recent Trends in Photoacoustic Imaging Techniques for 2D Nanomaterial-Based Phototherapy

Woo Yeup Jeong [1,†], Moon Sung Kang [2,†], Haeni Lee [2], Jong Hun Lee [3], Jeesu Kim [2,*], Dong-Wook Han [2,*] and Ki Su Kim [1,*]

[1] School of Chemical Engineering, College of Engineering, Pusan National University, Busan 46241, Korea; duq5315@naver.com
[2] Department of Cogno-Mechatronics Engineering, College of Nanoscience & Nanotechnology, Pusan National University, Busan 46241, Korea; mskang7909@gmail.com (M.S.K.); dovelet2@pusan.ac.kr (H.L.)
[3] Department of Food Science and Biotechnology, Gachon University, Seongnam, Gyeonggi 13120, Korea; foodguy@gachon.ac.kr
* Correspondence: jeesukim@pusan.ac.kr (J.K.); nanohan@pusan.ac.kr (D.-W.H.); kisukim@pusan.ac.kr (K.S.K.); Tel.:+82-51-510-6128 (J.K.); +82-51-510-7725 (D.-W.H.); +82-51-510-2496 (K.S.K.)
† These authors contributed equally to this work.

Abstract: A variety of 2D materials have been developed for therapeutic biomedical studies. Because of their excellent physicochemical properties, 2D materials can be used as carriers for delivering therapeutic agents into a lesion, leading to phototherapy. Various optical imaging techniques have been used for the monitoring of the treatment process. Among these, photoacoustic imaging has unique advantages including relatively deep imaging depth and large field of view with high spatial resolution. In this review article, we summarize the types of photoacoustic imaging systems used for phototherapy monitoring, then we explore contrast-enhanced photoacoustic images using 2D materials. Finally, photoacoustic image-guided phototherapies are discussed. We conclude that 2D material-based phototherapy can be efficiently monitored by photoacoustic imaging techniques.

Keywords: 2D materials; phototherapy; photoacoustic imaging; image-guided therapy

Citation: Jeong, W.Y.; Kang, M.S.; Lee, H.; Lee, J.H.; Kim, J.; Han, D.-W.; Kim, K.S. Recent Trends in Photoacoustic Imaging Techniques for 2D Nanomaterial-Based Phototherapy. *Biomedicines* **2021**, *9*, 80. https://doi.org/10.3390/biomedicine9010080

Received: 24 November 2020
Accepted: 13 January 2021
Published: 15 January 2021

1. Introduction

Two-dimensional nanomaterials with a well-ordered 2D planar structure (thickness > 100 nm) have been widely developed. Thanks to their beneficial biocompatible and biodegradable characteristics, various types of 2D nanomaterials, such as graphene derivatives; LDH, layered double hydroxide; TMD, transition metal dichalcogenide; TMO, transition metal oxide; and BP, black phosphorus, have been used for biomedical applications including drug delivery, tissue engineering, bio-imaging, and bio-sensing [1] (Figure 1). Because such materials have beneficial physicochemical properties of biocompatibility and degradability, they are suitable for biomedical applications including drug delivery, tissue engineering, bio-imaging, and biosensors [2–6]. Two-dimensional nanomaterials can cause a photothermal effect that generates heat by converting light energy into thermal energy when they are irradiated with near-infrared (NIR) light, and can then be used for phototherapy [7].

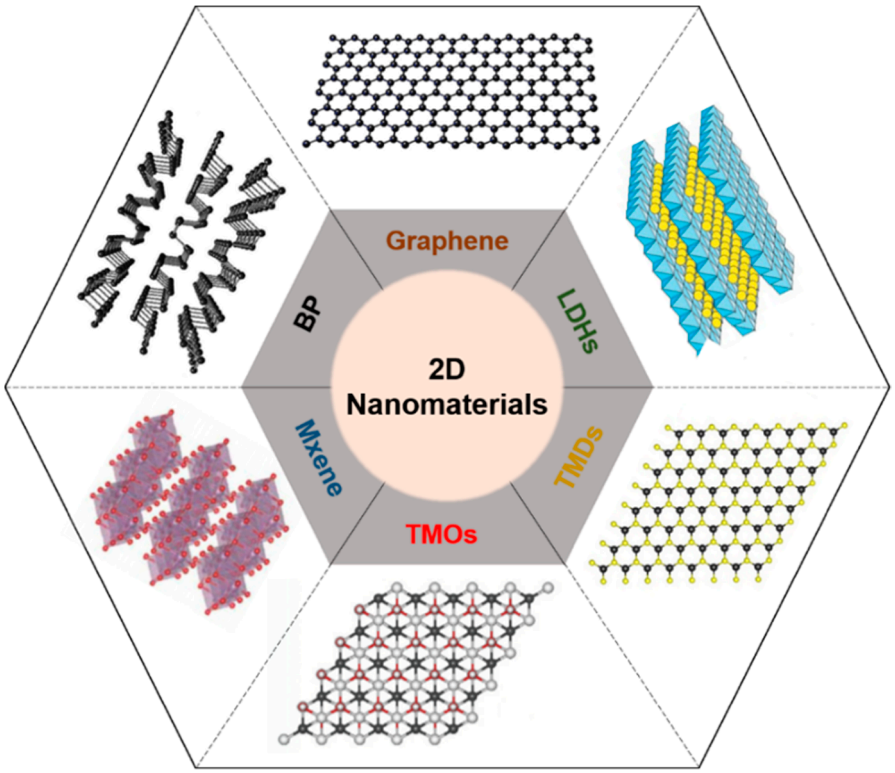

Figure 1. Schematic illustration of representative 2D nanomaterials. LDH, layered double hydroxide; TMD, transition metal dichalcogenide; TMO, transition metal oxide; BP, black phosphorus.

The representative phototherapy methods are photothermal therapy (PTT) and photodynamic therapy (PDT) [8]. In PTT, the local heating of NIR-absorbing agents is triggered by NIR light illumination. As tumor cells have difficulty dissipating heat, the NIR-triggered photothermal effect causes selective death of cancerous cells, which can be ablated more than 42 °C through necroptosis and apoptosis, which is programmed cell death, while endowing little damage to normal cells [9]. In contrast, PDT is an indirect method using photosensitizers that generate harmful singlet oxygen ($^1O_2$) when they absorb light. As PDT does not generate heat, nanomaterials in PDT usually perform as carriers that transfer photosensitizers using their surface properties [10]. To assess the therapy, drug delivery, and biodegradability, visualization of the internal biodistribution is essential.

Various biomedical imaging techniques, such as X-ray computed tomography (CT), magnetic resonance imaging (MRI), and positron emission tomography (PET), have been used for visualizing the distribution of nanomaterials, monitoring the delivery of nanomaterials, and assessing the efficacy of treatments [11–14]. Particularly, optical imaging techniques have been widely used as they provide high optical contrast, rich functional information, and excellent spatiotemporal resolution [15]. Compared with other biomedical imaging techniques, optical imaging systems can be implemented with low cost and simple configuration. In addition, optical imaging does not create harmful ionizing radiation, which makes the system favorable for future clinical translation. However, despite the advantages set out above, optical imaging is not widely used in clinics. The primary limitation of optical imaging is shallow imaging depth due to photon scattering in biological tissue [16].

Photoacoustic (PA) imaging is a biomedical imaging technique that combines the principles of ultrasound (US) and optical imaging [17]. The principle of PA imaging is based on the PA effect, which involves energy transduction from laser to acoustic waves through thermoelastic expansion (Figure 2). The typical procedure of PA imaging is as follows: (1) illumination of a short (typically a few nanoseconds) pulsed laser beam to target tissue, (2) light absorption and heat release by the optically absorbing chromophores, (3) acoustic

wave (i.e., PA wave) generation through rapid thermal expansion and relaxation, (4) signal reception using US transducer, and (5) image generation and display. Because PA imaging inherits the principles of optical and US imaging techniques, it can provide both strong optical contrast and high ultrasound resolution in deep tissue [18,19]. In addition to intrinsic chromophores (oxy- and de-oxy-hemoglobins, melanin, lipids, and water), external agents (organic dyes, liposomal nanoformulations, nanoparticles, and nanostructures) have been widely used to obtain contrast-enhanced PA images [20–23]. Moreover, using multiple wavelengths of the excitation laser, molecular functional information of biological tissue can be obtained, which can be used for investigating the bio-distribution of external agents in vivo [24–26].

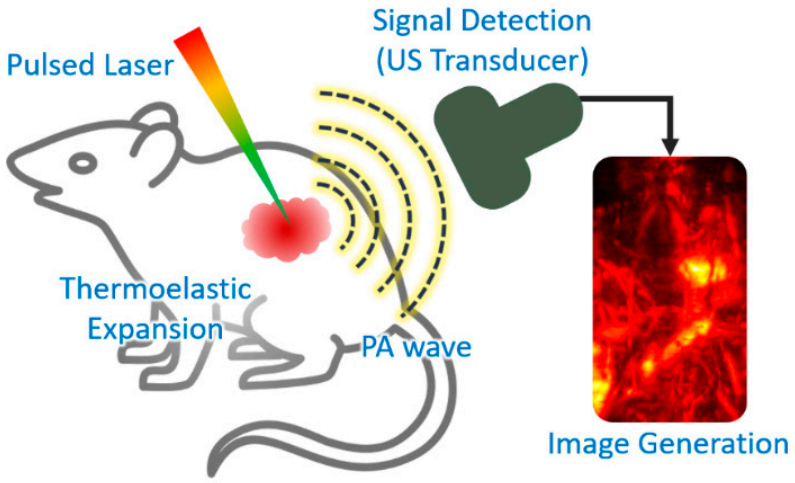

Figure 2. Schematic explanation of the procedure of PA imaging. PA, photoacoustic; US, ultrasound. The inset image is reproduced with permission from [27].

In this review article, we summarize several types of preclinical PA imaging systems for monitoring the distribution of nanomaterials in vivo. We also introduce recent trends and therapeutic applications of PA imaging for 2D material-based phototherapy. By monitoring the delivery and theranostic procedure, we can determine the future direction of PA imaging as an investigational tool for 2D nanomaterials.

2. Photoacoustic Imaging System

In general, PA imaging systems can be classified as PA microscopy (PAM) and PA computed tomography (PACT). The main difference between the two types of system is mathematical computation in the image reconstruction algorithm. In PAM, a single-element transducer is used to achieve PA signals along the depth direction (i.e., A-line signal) at the top of the sample, thus no mathematical reconstruction algorithm is required. In contrast, PACT utilizes rotational scanning methods or multi-element US transducers to acquire tomographic information regarding the target. Therefore, PACT requires image reconstruction algorithms [28–30]. Compared with PACT, PAM systems have higher resolutions, but suffer from shallow imaging depth and slow imaging speed.

2.1. Photoacoustic Microscopy

PAM can be divided into two types: optical-resolution PAM (OR-PAM) and acoustic-resolution PAM (AR-PAM). OR-PAM uses tight optical focus, ~10 times smaller than acoustic focus, while the emphasis of AR-PAM is to tighten the acoustic focus. In OR-PAM, the lateral resolution is determined by the optical focal spot size, which depends on the numerical aperture of an objective lens (Figure 3A). The tightly focused optical beam excites optically absorbing chromophores only in the focal zone (red dot in Figure 3A), and the PA waves are generated from the excited chromophores. Because the optical focal spot is smaller than the acoustic focal spot, all the generated PA waves are detected

by the US transducer (black arrow in Figure 3A). We can note that PA waves are not generated from the unexcited chromophores (orange dots in Figure 3A), which leads to the better resolution of OR-PAM compared with AR-PAM. In contrast, the resolution of AR-PAM is determined by the acoustic focal size because the optical focal spot is larger than the acoustic focal spot (Figure 3B). The size of the acoustic focal spot depends on the characteristics of the US transducer. The widely delivered optical beam excites chromophores in a large area (red dots in Figure 3B), then generates PA waves (black and gray arrows in Figure 3B). Among them, the PA waves in the acoustic focal zone (black arrows in Figure 3B) are detected by the ultrasound transducer. Therefore, the acoustic focus determines the resolution of the system.

By adjusting the optical focus, the resolution of OR-PAM can be greatly improved (Figure 3C) [31–35]. However, imaging depth can be limited because maintaining tight optical focus is difficult while scanning the imaging area. Therefore, compared with AR-PAM, OR-PAM systems usually have a small field of view (FOV) and a shallow imaging depth. As a tight optical focus is not required, AR-PAM has the advantage of being able to image deeper and larger areas in biological tissues compared with OR-PAM (Figure 3D) [36–41].

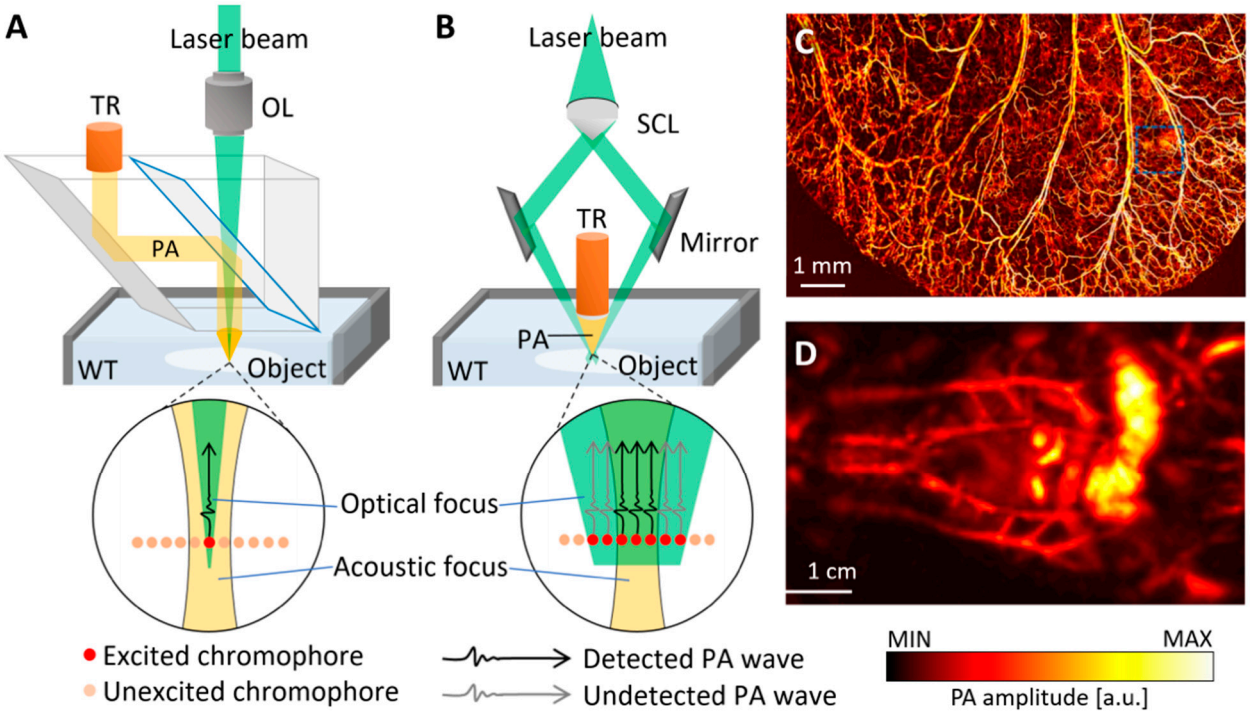

Figure 3. Schematic illustration and representative images of OR- and AR-PAM systems. The typical configurations of (**A**) OR-PAM and (**B**) AR-PAM. The optical focus is smaller than the acoustic focus in OR-PAM, while the optical focus is larger than the acoustic focus in AR-PAM. The red and orange dots are excited and unexcited chromophores, respectively. The black and gray arrows are detected and undetected PA waves, respectively. (**C**) PA images of mouse ear acquired using an OR-PAM. (**D**) PA images of the whole body of mouse acquired using an AR-PAM. OR-PAM, optical resolution photoacoustic microscope; AR-PAM, acoustic resolution photoacoustic microscope; PA, photoacoustic; TR, ultrasound transducer; WT, water tank; OL, objective lens; SCL, spherical conical lens. The images are reproduced with permission from [31,39].

2.2. Photoacoustic Computed Tomography

For further enhancement of FOV and imaging speed, PA computed tomography (PACT) using array transducers has been introduced (Figure 4) [42–45]. Using multi-element transducers with various geometrical structures (linear, arc, planar, or hemispherical arrays), PACT can achieve PA signals at multiple positions with a single laser shot; therefore, the imaging speed and FOV can be significantly enhanced [45–49]. For potential

clinical applications, clinical US machines have been used for PACT. As the receiving signals of both PA and US are acoustic waves, the signal acquisition and image reconstruction procedures of the two imaging techniques are identical, and they can thus share a single imaging platform [27,50–52]. Combined PA and US images, providing complementary structural and functional information regarding biological tissues, have been investigated in clinical applications such as melanoma detection, cancer classification, and vascular disease assessment [53–56].

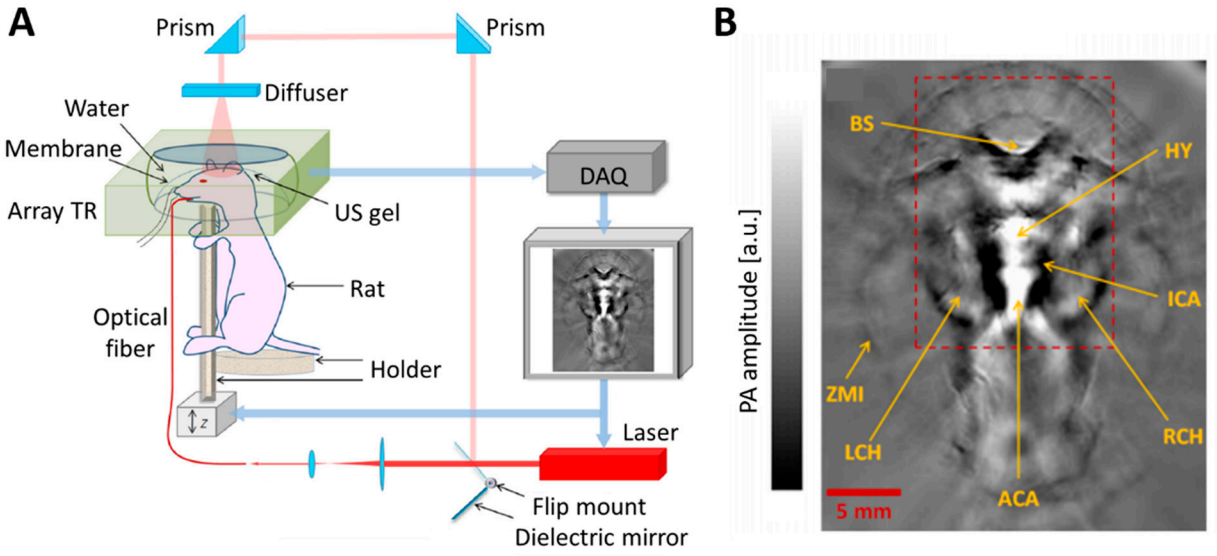

Figure 4. Schematic illustration and representative images of a PACT system. (**A**) Typical configurations of PACT. Array transducer is used to acquire PA images. (**B**) Representative PACT images of mouse brain in vivo. PA, photoacoustic; PACT, photoacoustic computed tomography; TR, ultrasound transducer; US, ultrasound; DAQ, data acquisition module; BS, brain stem; HY, hypothalamus; ICA, internal carotid artery; LCH, left cerebral hemisphere; RCH, right cerebral hemisphere; ACA, anterior cerebral artery; ZMI, zygomatic muscle interface. The images are reproduced with permission from [42].

2.3. Performance Benchmarks of Photoacoustic Imaging Systems

As each type of system has complementary advantages in terms of imaging depth, spatial resolution, imaging speed, and FOV, a variety of PA imaging systems have been applied in biomedical studies including the monitoring of phototherapy. The typical performances of PA systems are summarized in Table 1. OR-PAM has an excellent spatial resolution in a shallow depth of biological tissue, thus it is usually utilized for visualization of superficial regions such as the ear, eye, or peripheral vasculature. AR-PAM can obtain a signal that penetrates deeper into biological tissue and an extended FOV compared with OR-PAM, as is used for monitoring the whole-body distribution of nanomaterials, drugs, or contrast agents. PACT further extends FOV and imaging speed, thus it can monitor the real-time response of biological tissue during treatment using nanomaterials.

Table 1. Performance benchmarks of representative PA imaging systems. PA, photoacoustic; OR-PAM, optical resolution photoacoustic microscopy; AR-PAM, acoustic resolution photoacoustic microscopy; PACT, photoacoustic computed tomography; FOV, field of view.

Type	Lateral Resolution	Axial Resolution	Imaging Depth	Imaging Time	FOV	Ref.
OR-PAM	2.56 μm	-	1.2 mm	70 min	7.8 × 10 mm^2	[31]
	3.6 μm	27.7 μm	1 mm	7 s	9 × 4 mm^2	[34]
	2.7 μm	46.4 μm	400 μm	4 min	6 × 8 mm^2	[35]
AR-PAM	590 μm	150 μm	25 mm	20 min	60 × 32 mm^2	[39]
	45 μm	33 μm	7.6 mm	10 min	9 × 7 mm^2	[40]
	84 μm	38 μm	2.3 mm	224 s	36 × 80 mm^2	[41]
PACT	250 μm	100 μm	13 mm	16 s	25 × 30 mm^2	[42]
	1.5 mm	-	10 mm	0.1 s	20 × 20 mm^2	[44]
	1.2 mm	205 μm	30 mm	0.2 s	40 × 60 mm^2	[27]

3. Phototherapy Using 2D Nanomaterials

3.1. Types and Characteristics

Currently, various phototherapy agents including gold nanostructures [57,58], mesoporous silica nanoparticles [59,60], and 2D nanomaterials have been widely investigated for clinical application. Among them, 2D nanomaterials are attracting the most attention because they can be used not only for phototherapy, but in other biomedical fields thanks to their excellent biochemical properties (Table 2). Typical 2D nanomaterials consist of one or a few atomic layers. As a representative 2D nanomaterial, graphene has a honeycomb structure consisting of carbon atoms. By changing the shape, the number of layers, and chemical modifications, several derivatives can be formed. Among them, graphene oxide (GO) [57] and reduced graphene oxide (rGO) [58,59] have been widely utilized for biomedical applications because of their superior electrical and thermal conductivities, large surface area, chemical versatility, and biocompatibility [60–62]. Layered double hydroxides (LDHs) are inorganic 2D nanomaterials with structures in which metal atoms are sandwiched by hydroxide layers. Because of their high charge density with excellent biocompatibility, LDHs are widely used as nano-carriers for theranostic agents in drug or gene delivery, phototherapy, and immunotherapy [63–65]. Transition metal dichalcogenides (TMDs) have hexagonal lattices consisting of monolayers of transition metal atoms between chalcogen atom layers. In addition to thin, flexible, and strong characteristics, TMDs are excellent optical absorbers, thus producing photolimunescence and photothermal effects [66–69]. TMDs can be formed with various materials including molybdenum disulfide (MoS_2) [70–73], tungsten disulfide (WS_2) [74–77], and molybdenum diselenide ($MoSe_2$) [78–80]. Transition metal oxides (TMOs) are compounds of oxygen atoms and transition metals such as titanium (TiO_2) [81,82] and manganese (MnO_2) [83–85]. Their wide bandgap results in excellent photochemical and electric properties [86,87]. They can also directly interact with drugs, genes, or other biomolecules by surface modification and thus can be utilized in biomedical applications including drug delivery, cancer therapy, tissue engineering, bio-imaging, and biosensing [88–90]. Mxenes are the most recently discovered 2D materials and have been applied in various biomedical applications because of their extreme thinness, large surface area, high surface–volume ratio, and mechanical strength [91–95]. Black phosphoruses (BP) are the most stable allotropes of phosphorus with zigzag or armchair bilayer structures. BP have shown potential in biomedical applications with their strong optical absorption in the ultraviolet (UV) and NIR regions [96–100]. They have also demonstrated promising biocompatibility and biodegradation [101].

3.2. Phototherapy Using 2D Nanomaterials

By taking advantage of their strong optical absorption and thermal transition properties, 2D nanomaterials have been used for PTT. Liu et al. successfully prepared a doxoru-

bicin (DOX)-loaded MoS_2-PEG nanosheet for combined PTT–chemo cancer therapy [102]. In that study, nanosheets were analyzed for drug delivery and photothermal effects by NIR irradiation. MoS_2-PEG/DOX nanosheets exhibited synergistic anti-cancer effects, inhibiting tumor growth in in vivo experiments. Zeng et al. reported on ultrathin MnO_2 nanosheets of polyethylene glycol-cyclic arginine-glycineaspartic acid tripeptide (PEG-cRGD) and encapsulated chlorin e6 (Ce6) for PTT/PDT synergistic cancer therapy (Figure 5) [103]. In that study, the nanosheets showed photothermal efficiency of 39% and could be reduced by overexpressed acidic H_2O_2, which could efficiently generate O_2 and further enhance the therapeutic efficiency of PDT. Moreover, the MnO_2-PEG-cRGD/Ce6 exhibited pH-controlled and NIR-induced Ce6 release, and showed favorable therapeutic outcomes under a single 660 nm NIR laser.

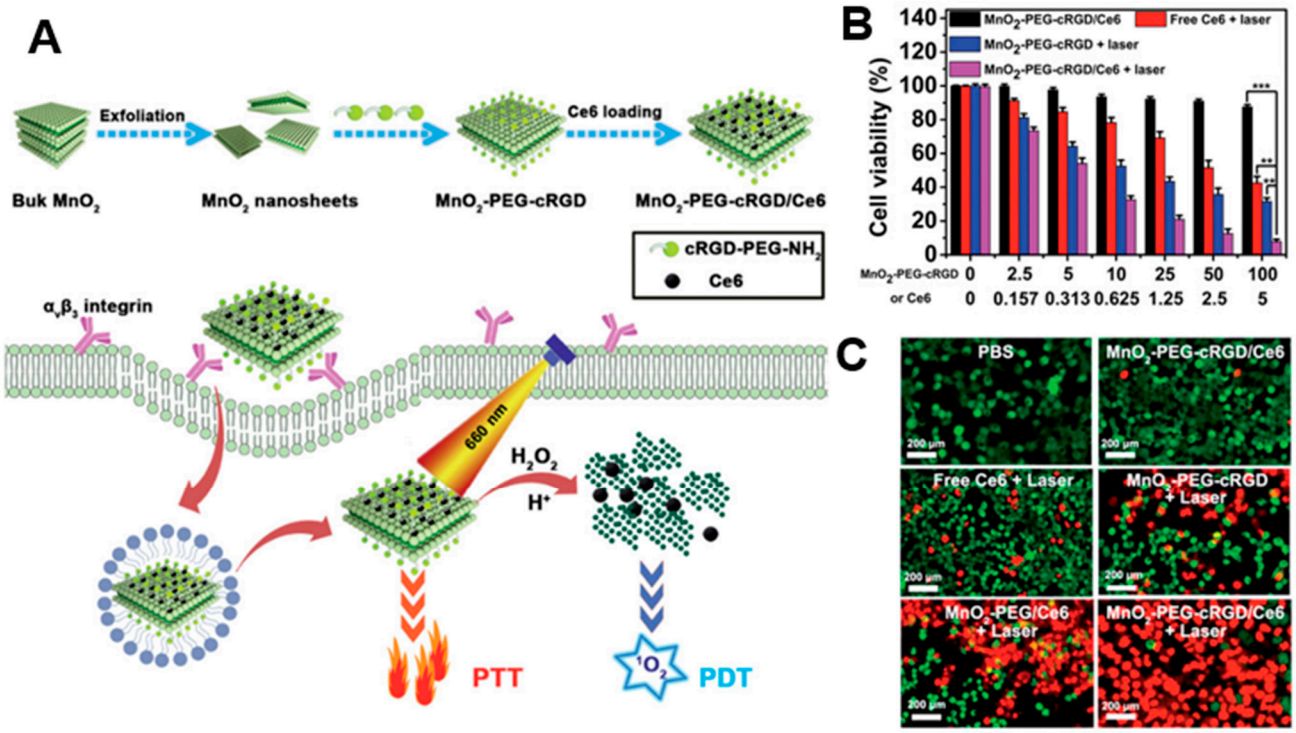

Figure 5. (**A**) Schematic illustration for the preparation of MnO_2-PEG-cRGD/Ce6 for synergistic photothermal/photodynamic (PTT/PDT) therapy. (**B**) Relative viabilities of PC3 cells after incubation with free Ce6, MnO_2-PEG-cRGD with 660 nm light irradiation, or MnO_2-PEG-cRGD/Ce6 with or without 660 nm light irradiation (0.6 W cm^{-2}, 10 min, *** $p < 0.001$, ** $p < 0.01$). (**C**) Fluorescence images of calcein acetoxymethyl ester (Calcein-AM, green)/propidium iodide (PI, red) double stained cells after different treatments. The images are reproduced with permission from [103].

A number of PDT studies have investigated the development of 2D nanomaterials that release photosensitizers. Moosavi et al. prepared N-TiO_2 nanoparticles to generate reactive oxygen species (ROS) and induce autophagy [81]. They showed the dose-dependent capability of well-dispersed photo-activated N-TiO_2 NPs to induce terminal megakaryocyte differentiation and cell death in K562 leukemia cells. In cellular experiments, N-TiO_2 nanoparticles increased ROS levels with light irradiation. Yang et al. fabricated covalently, incorporating both chlorin e6 (Ce6) and triphenyl phosphonium (TPP) onto BP@PDA NSs for dual-modal imaging-guided synergistic photothermal and photodynamic therapy (Figure 6) [104]. BP@PDA–Ce6&TPP NSs can produce considerable heat, mainly owing to BP@PDA NSs, and can generate sufficient ROS for PDT. With these results, BP@PDA–Ce6&TPP NSs can be used for PTT/PDT therapy of cancers.

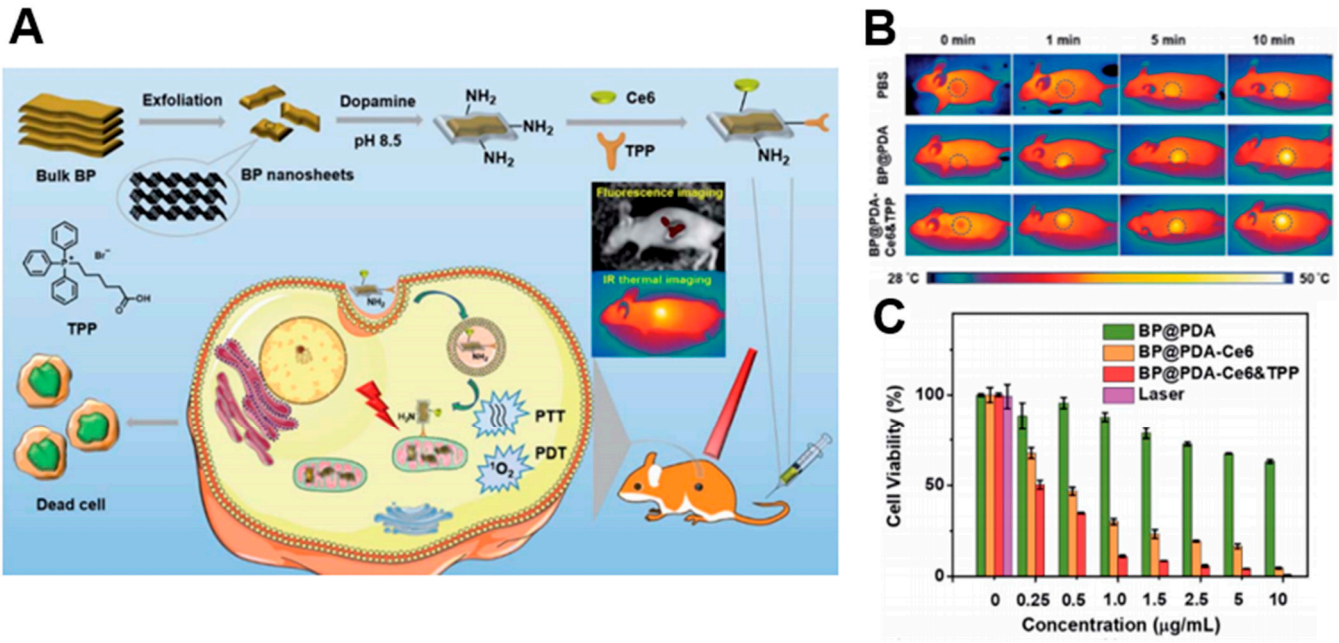

Figure 6. (**A**) Schematic illustrations of the preparation, therapeutic uses, and peaks in functions of BP@PDA–Ce6&TPP NSs. (**B**) Ex vivo fluorescence imaging of main organs as well as tumor at 24 h post-injection. (**C**) Relative viabilities of HeLa cells incubated with BP@PDA NSs, BP@PDA–Ce6 NSs, and BP@PDA–Ce6&TPP NSs at different BP@PDA concentrations with laser illumination (660 nm, 0.5 W cm^{-2}, 5 min). Data represent mean ± SD (n = 4). The images are reproduced with permission from [104].

Table 2. Phototherapy using 2D nanomaterials. PTT, photothermal therapy; PDT, photodynamic therapy.

2D Nanomaterials	Photothermal Conversion	Therapy	Applied Forms	Ref.
Graphene derivatives	63% (G), 35% (GO) [59]	PTT, PDT PTT	GO-UCNPs-ZnPc GO/$MnFe_2O_4$/DOX	[61] [62]
TiO_2	40.8% [86]	PTT PDT	Ag@TiO_2 N-TiO_2	[82] [81]
MoS_2	0.84% [67]	PTT PTT, PDT PTT	MoS_2-HA-DTPA-Gd AuNBPs@MoS_2 MoS_2-Gd-BSA	[71] [72] [73]
BP	30.84% [97]	PTT PTT PTT, PDT	BP-Au NSs BP-PEG-FA/Cy7 NSs BP@PEG/Ce6 NSs	[98] [99] [100]
Mxene(Ti_3C_2)	≒ 100% [92]	PTT PTT, PDT PTT, PDT	Ti_3C_2@Au Ti_3C_2-SP Ti_3C_2-DOX	[93] [94] [95]
WS_2	35% [68]	PTT, PDT PTT PTT	BSA-WS_2@MB WS_2-PEG WS_2-IO/S@MO-PEG	[75] [76] [77]
$MoSe_2$	54.3% [69]	PTT, PDT PTT, PDT	$MoSe_2/Fe_3O_4$ $MoSe_2$@PEG-Dox	[79] [80]
2D Boron	42.5% [104]	PTT, PDT	B@Ce6–PAH–PAA	[105]
MnO_2	62.4% [87]	PTT PTT	MnO_2-PEG-FA/DOX BSA-MnO_2 NPs	[84] [85]

4. Photoacoustic Image-Guided Phototherapy

4.1. Contrast-Enhanced Photoacoustic Imaging Using 2D Nanomaterials

PA imaging, one of the latest and most promising imaging modalities, has been shown to enable visualization of tissues with centimeter-depth penetration for in vivo imaging (Table 3). However, the optical contrast ratio of tissues is generally low; therefore, conventional PAI can only detect specific tissues that have strong absorbance. However, certain kinds of imaging probes can be utilized to enhance the optical contrast ratio of tissues with low absorbance. Specifically, incorporating 2D NMs that strongly absorb light in the tissues to be irradiated can overcome the inherently low contrast problem. When incorporating 2D NMs exhibiting PT properties into tissues with low contrast, they absorb light more than the surrounding tissue components, hence emitting a stronger PA signal.

Table 3. Recent photothermal (PT)-Photoacoustic Imaging(PAI) multimodal studies classified by their characteristics.

PT-Multimodality	Key Material	Formulation	Modification/Functionalization/Hybridization	Experimental	Ref.
x	Black phosphorus (BP)	Quantum dot	Sulfonic ester of the titanium ligand (TiL4)	MCF-7, 293T cells, and MCF-7 tumor-bearing Balb/c nude mice	[103]
	Layered double hydroxide (LDH)	Nanosheet	CoMn and chlorin e6 (Ce6)	HeLa, U87mg, HepG2, 4T1 cells, and HeLa tumor-bearing Balb/c nude mice	[106]
	Reduced graphene oxide (rGO)	Nanocomposite	Polyethylene glycol (PEG), indocyanine green (ICG)	Hela cells, Balb/c nude mice	[107]
o	Antimonene (AM)	Liquid phase nanoflake	PEG	293T, MCF-7, SK-BR3, T47D cells, and MCF-7 tumor-bearing mice	[108]
	Antimony (III) Selenide (Sb_2Se_3)	Nanosheet	Poly(vinyl pyrrolidone) (PVP)	4T1, MBA-MD-231 cells, Balb/c nude mice	[109]
	Tantalum carbide (Ti_3C_2 MXene)	Nanosheet	SP (soybean phospholipid) and doxorubicin (DOX)	4T1 cells, 4T1-inoculated mice	[94]
	Tantalum carbide (Ta_4C_3 Mxene)	Nanosheet	MnO, SP	4T1 cells, Kunming mouse, 4T1 tumor-bearing mice, and Balb/c nude mice	[110]
	MXene (Ta_4C_3)	Nanosheet	Manganese oxide nanoparticles (MnO_x) and SP	4T1 cells and 4T1 tumor-bearing nude mice	[111]
	Bismuth selenide (Bi_2Se_3)	Nanosheet	None	MCF-7 cells and MCF-7 tumor-bearing Balb/c nude mice	[112]
	Bi_2O_2Se	Quantum dot	None	A549, MCF-7 cells, and MCF-7 tumor-bearing Balb/c nude mice	[113]
	Bi_2Se_3	Nanodish	HA, polypyrrole (PPy), and zinc phthalocyanine (ZnPc)	4T1 cells and 4T1 tumor-bearing Balb/c nude mice	[114]
	Molybdenum disulfide (MoS_2)	Nanoconjugate	Hyaluronic acid (HA)	HCT116 cells and HCT116-inoculated mice	[115]
	MoS2	Nanosheet	Iron oxide nanoparticle (IONP) and PEG	Balb/c mice and 4T1 tumor-bearing mice	[116]
	MoS_2 and Bi_2S_3	Nanosheet	PEG	L929 cells and 4T1 tumor-bearing Balb/c nude mice	[117]
	Palladium (Pd)	Nanosheet	DOX, Zeolitic imidazolate frameworks (ZIF-8), Polydopamine (PDA)	WBCs (white blood cells) from mice, 4T1 cells, and 4T1 tumor-bearing mice	[118]
	Pd	Nanoplate	Au and PEG	4T1 tumor-bearing Balb/c mice	[119]
	Titanium (Ti)	Nanosheet	PEG	SMMC-7721, B16, J774A.1 cells, and Balb/c nude mice	[120]
	Germanene	Quantum dot	PEG	MCF-7, 4T1, H1299, HeLa cells, and Balb/c mice	[121]

Table 3. *Cont.*

PT-Multimodality	Key Material	Formulation	Modification/Functionalization/Hybridization	Experimental	Ref.
	Boron	Nanosheet	PEG	HeLa, PC3, MCF-7, A549 cells, and MCF-7 tumor-bearing mice	[104]
	Manganese boride	Nanosheet	Bi	4T1 cells and 4T1 tumor-bearing mice	[122]
	MnO_2	Nanosheet	None	U87MG cells and U87MG tumor-bearing mice	[123]
	Tungsten disulfide (WS_2)	Nanosheet	PVP	L929, HT29 cells, KM mice, and HT29 tumor-bearing KM mice	[124]
	Co_9Se_8	Nanoplate	Poly(acrylic acid) (PAA), DOX	HepG2 cells, HepG2 tumor-bearing Balb/c-nude mice	[125]
	Au	Nanoring	None	Raw 264.7 cells, U87MG tumor-bearing nude mice	[126]
	Cu_2MnS_2	Nanoplate	Monomethoxycarboxyl polyethylene glycol (mPEG-COOH)	HeLa, S180 cells, and S180 tumor-bearing Balb/c nude mice	[127]

BP is a newly emerging 2D nanomaterial that exhibits a layer-dependent bandgap, resulting in versatile properties for electronic and optoelectronic application. However, BP is highly reactive to oxygen and water, hence its physical properties, biodistribution, and optical properties can be altered in an in vivo environment. Several studies have focused on the stabilization of BP for PA applications. Sun et al. fabricated TiL4-coordinated BPQDs (TiL_4@BPQDs) for PA imaging of cancer [103]. TiL_4 enhanced the stability of BPQDs in aqueous dispersions and maintained optical properties for a prolonged time compared with bare BPQDs. A PA signal was observed from the MCF-7 cells after the addition of only 12.5 ppm of TiL4@BPQDs, which is only 0.63% of the common imaging dose of 2 mg/L, suggesting their high sensitivity in in vitro PA imaging (Figure 7A). Moreover, the in vivo PA images indicated a sixfold increase in PA signal at 680 nm after injection of TiL4@BPQDs into xenografted tumors in mice (Figure 7B), which was superior to the signal generated by Au nanorods (a common PA exogenous probe). These results suggest the potential of BP for PA imaging if the unstable in vivo properties can be resolved by surface modification.

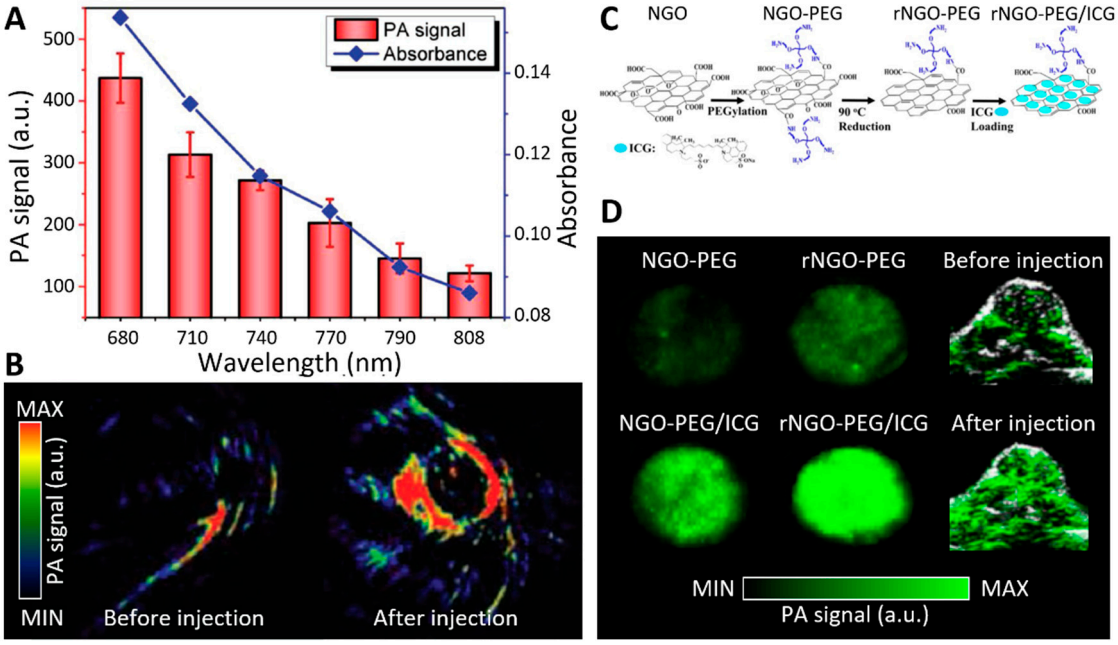

Figure 7. (**A**) In vitro PA signals and optical absorbances of TiL_4-coordinated black phosphorus quantum dots (BPQDs) with various excitation wavelengths. (**B**) In vivo PA images of MCF-7 tumor xenografted Balb/c mice before and after intravenous injection of TiL_4-coordinated BPQDs. (**C**) Schematic diagram of ICG-rGO nanocomposite preparation. (**D**) In vitro and in vivo PA signals of ICG-rGO nanocomposites with an excitation wavelength of 780 nm. The in vivo images of HeLa tumor inoculated Balb/c nude mice were acquired before and after tail vein injection of rNGO-PEG/ICG. PA, photoacoustic; NGO, nano-graphene oxide; rNGO, reduced nano-graphene oxide; PEG, polyethylene glycolated; ICG, indocyanine green. The images are reproduced with permission from [103,107].

Tumor targetability is one of the most promising strategies for enhancing the PA signal in cancer imaging. The tumor microenvironment (TME) is characterized by high H_2O_2 and glutathione (GSH) levels, low pH value, and hypoxia; therefore, the incorporation of TME-responsive NM suggests potential for tumor-specific PAI. Yan et al. introduced Ce6-modified CoMn-LDH nanosheets for an enhanced tumor microenvironment response [106]. The CoMn-LDH nanosheets exerted complete quenching of $^1O_2$ generation by the browning of the particle. The results indicated a good linear correlation between PA signal intensity and Ce6/CoMn-LDH concentration within 0–100 μg/mL. In vivo injection of the Ce6/CoMn-LDH nanosheets produced a weak signal that was observed after 2 h injection and increased gradually from 2 to 12 h after injection, indicating the accumulation of Ce6/CoMn-LDH nanosheets in the tumor area. The results demonstrated that Ce6/CoMn-

LDH nanosheets accumulated in the tumor owing to the enhanced permeability and retention (EPR) effect, which presented as PA-combined multimodal imaging agents.

rGO, a derivative of graphene, has also been adopted as a promising PA probe thanks to its high drug loading capacity and optical absorption property in the NIR regime. Chen et al. fabricated an indocyanine green (ICG)-conjugated rGO nanocomposite for dual use of PAI and fluorescence imaging (Figure 7C) [107]. The nanocomposite was shown to exhibit little toxicity and high PA/fluorescence signals both in vitro and in vivo (Figure 7D). ICG-rGO nanocomposites showed high cytocompatibility at a concentration of 100 μg/mL and there was no obvious tissue damage in the heart, liver, spleen, kidney, or lung after injection of the particle. Moreover, ICG-rGO nanocomposites induced 63.5% of cellular uptakes and then exhibited strong red fluorescence. In vivo fluorescence imaging and PA imaging also demonstrated that ICG-rGO nanocomposites accumulated in the tumor and significantly enhanced the imaging contrasts. rGO is considered a promising candidate as a multimodal imaging probe for cancer diagnosis.

4.2. Photoacoustic Imaging for Monitoring Phototherapy

As an emerging phototheranostic modality, interest in PA-combined PTT has increased in recent tumor treatment research [76,128–130]. After PAI provides guidance towards the tumor site and reveals strong tumor contrast after injection, the targetability and efficiency of PTT can be significantly increased (Figure 8). Several 2D nanomaterials have multimodal characteristics with PT and PA properties; therefore, they have been extensively studied for PAI-guided PTT. AM, the 2D layered material exfoliated from bulk antimony (Sb), has been highlighted because of its superior physicochemical properties compared with typical 2D nanomaterials such as graphene, MoS_2, WS_2, and BP [131]. Yu et al. fabricated liquid phase exfoliated AM nanoflakes (AMNFs) exhibiting unique PA properties, making AMNFs superior to both other 2D materials, such as BP, GO, and TMDs, and commonly used PA contrast agents, such as indocyanine green (ICG) and gold nanorods (AuNRs) [108]. The AMNFs exhibited 42.36% PT conversion efficiency, which was about two times higher than other 2D NMs (e.g., GO 25%, BP 28%, MoS_2 28%, AuNRs 21%). The PA performance of 1000 μg/mL AMNFs exhibited a limit of detection (LOT) of 7.4×10^4 cells, which correlates with a 0.74 mm^3 tumor. It is known that about 85% of the human tumor is composed of 10^8 cells of 1 cm^3 [132]. Therefore, it can be demonstrated that the PA performance of the AMNFs is very sensitive. Sb_2Se_3, a chalcogenide formed from antimony and selenium, has also emerged as a promising PA-PT multimodal agent thanks to its attractive properties such as a proper optical bandgap (1.1–1.3 eV), high light absorption coefficient, low toxicity, and abundant material reserves [133]. However, Sb_2Se_3 has a unique crystal structure that inherently tends to grow into a one-dimensional structure, which makes it difficult to fabricate Sb_2Se_3 with the desirable 2D planar nanostructure. Zhou et al. reported on the construction of Sb_2Se_3 nanosheet highly efficient PA-guided PTT agents by NIR laser activation on mice with 4T1 tumor cells were inoculated on their thigh (Figure 8) [109]. The Sb_2Se_3 nanosheets were fabricated using liquid nitrogen pretreatment and a freeze–thawing approach, resulting in a high PT-conversion capability agent (extinction coefficient: 33.2 L/g·cm; photothermal conversion efficiency: 30.78%). Moreover, the poly(vinyl pyrrolidone) (PVP) surface engineering enhanced the biocompatibility and physiological stability, which led to a prolonged and 7.3 times increased PA signal after 6 h of in vivo injection compared with that of the initial value of the tumor. AM-based 2D NMs are promising PT-PA agents, possessing great PA properties and PT-conversion efficiency.

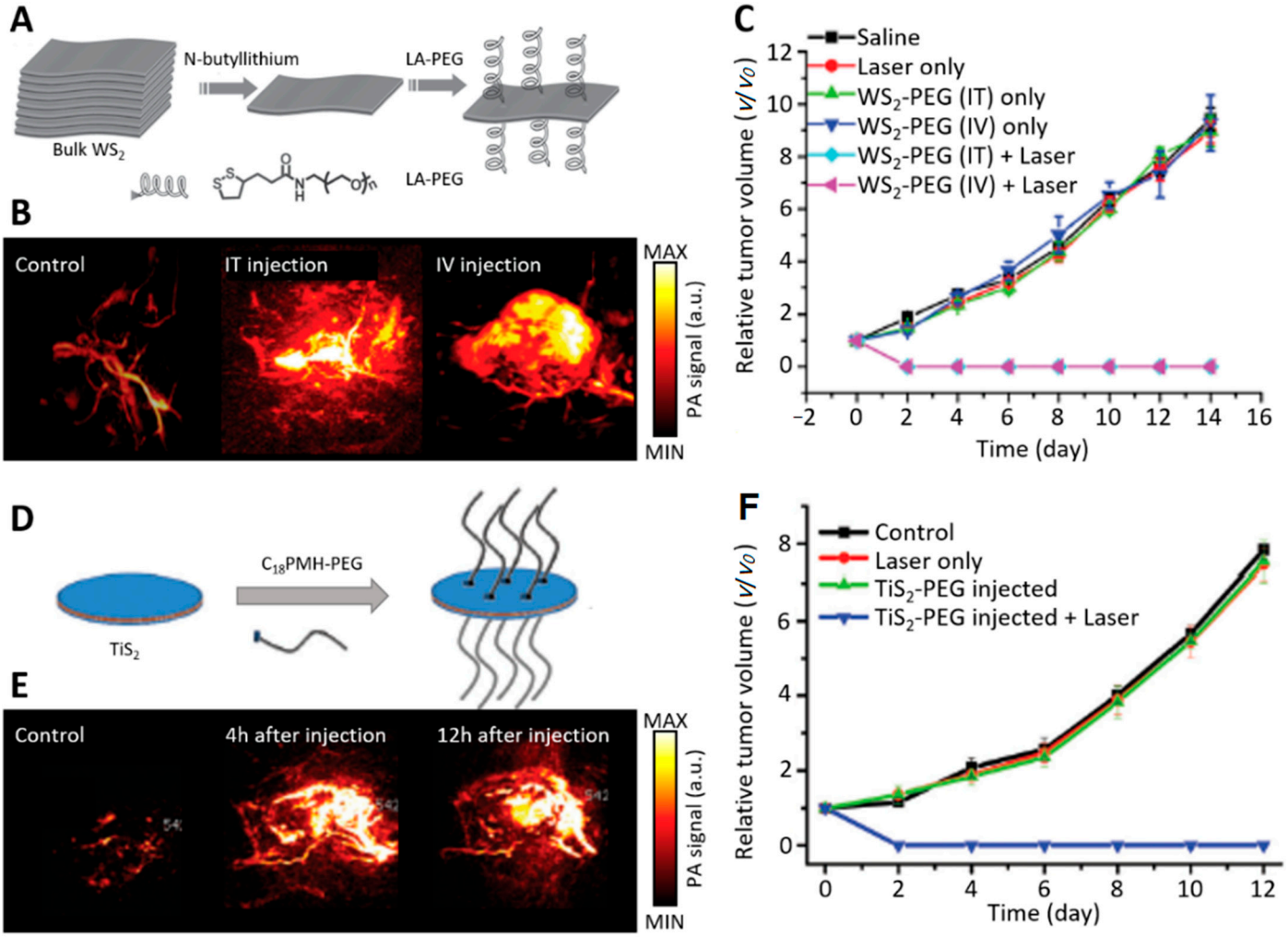

Figure 8. (**A**) Schematic diagram of exfoliation and PEGylation of WS_2 nanosheets. (**B**) In vivo PA images of 4T1 tumor bearing Balb/c mice before, after IT injection, and after IV injection of WS_2 nanosheets. (**C**) The growth of 4T1 tumors in different groups of mice after various treatments indicated. The relative tumor volumes were normalized to their initial sizes. (**D**) Schematic diagram of TiS_2-PEG nanosheets. (**E**) In vivo PA images of 4T1 tumor bearing Balb/c mice before, 4 h after, and 12 h after IV injection of TiS_2-PEG solution. (**F**) The growth of 4T1 tumors in different groups of mice after various treatments indicated. The relative tumor volumes were normalized to their initial sizes. PA, photoacoustic; IT, intratumoral; IV, intravenous. The images are reproduced with permission from [76,128].

The direct exfoliation of 2D ultrathin ceramic nanosheets from layer-structured solid and hard MAX-phase ceramics has been introduced, which has been termed MXene by Gogosti et al. [134]. The ultrathin planar structure of MXene endows the sheets with a large surface area, providing not only abundant anchoring sites for therapeutic drugs, but also high PT and PA conversion efficiency. Han et al. explored the PA and PT performances of Ti_3C_2 Mxene [94]. These Ti_3C_2 MXenes exhibited a PA signal at an excitation wavelength of 808 in vitro and a significant increase in PA signal at a concentration of 15 mg/kg (particles per 4T1-beared tumor), indicating the potential for PAI-guided therapy. Ti_3C_2 Mxene also showed high in vivo compatibility and easy excretion out of the body, suggesting potential high biosafety for further clinical translation. However, MXenes are limited in respect to their use as diagnostic imaging agents because of their simple material composition. Several studies have been carried out to endow them with specific functionality for theranostic application. Dai et al. fabricated SP-modified MnOx/Ta_4C_3-based nanosheets [111]. The PT-conversion performance of the SP-MnOx/Ta_4C_3 composite nanosheets showed fast enhanced PA signals (highest optical density at 15 min) after subcutaneous administration

in 4T1 tumor-bearing mice. Moreover, the SP-MnOx/Ta_4C_3 nanosheets exhibited contrast-enhanced properties in both CT and MR, suggesting the potential use of SP-MnOx/Ta_4C_3 nanosheets for multiple imaging tool-guided therapy.

As the other class of 2D-layered NMs, Bi_2Se_3 has been highlighted as a remarkable thermoelectric and photoelectric agent possessing suitable bioactivity and biocompatibility [135–137]. Xie et al. fabricated PVP-encapsulated Bi_2Se_3 nanosheets possessing an extinction coefficient of 11.5 L/g·cm at 808 nm, showing a PT conversion efficiency of 34.6% and excellent photoacoustic performance (about a twofold increase after 5 h of injection) [112]. The PVP-Bi_2Se_3 nanosheets showed high cytocompatibility in vitro (about 95% of cell viable after 48 h of 200 ppm PVP-Bi_2Se_3 treatment) and almost perfect in vivo clearance (in the liver, spleen, kidney, lung, and heart) after 30 days of intravenous injection.

MoS_2, one of the novel 2D nanomaterials, exhibits unique visible photoluminescence with high absorption in the NIR range. Despite the superior optical properties, the use of MoS_2 nanosheets for in vivo theragnosis agents is hampered by their instability and low intracellular delivery efficiency [138,139]. To overcome these issues, Shin et al. introduced HA-conjugated MoS_2 nanosheets to induce HA receptor-mediated endocytosis of the nanosheets [115]. HA is one of the biopolymers used for cancer cell-specific targeting because overexpressed cancer cell receptors such as cluster determinant 44 (CD44), hyaluronan receptor for endocytosis (HARE), and lymphatic vessel endothelial hyaluronan receptor-1 (LYVE-1) are reactive to the HA [140,141]. Therefore, HA-MoS_2 conjugates experience receptor-mediated endocytosis and intracellular disulfide cleavage by pH and GSH, and subsequently, HA degrades and MoS_2 nanosheets accumulate in the cells. In this method, PAI in tumor-bearing mice showed a 1860-fold increase in PA signal compared with control groups, which resulted from the high light-to-heat conversion efficiency of HA-MoS_2.

Pd nanosheets, as typical 2D nanomaterials with well-defined and controllable sizes, are promising candidates in PA-guided PTT owing to their strong NIR absorption and excellent biocompatibility [142–144]. Zhu et al. conjugated DOX, Pd, and ZIF-8 in a self-assembled one-pot method, and coated them with PDA to improve biocompatibility (DOX/Pd@ZIF-8@PDA) [118]. The prepared DOX/Pd@ZIF-8@PDA showed a ninefold increase in PA signal after 400 ppm NMs were injected in tumor-bearing mice. Moreover, as the concentration increased from 0 to 800 ppm, the temperature rose from 25 to 54 °C after 808 nm laser irradiation, indicating a high PT conversion efficiency for DOX/Pd@ZIF-8@PDA. Interestingly, the introduction of an 808 nm laser could significantly accelerate the release of DOX from DOX/Pd@ZIF-8@PDA. Hence, DOX/Pd@ZIF-8@PDA can be adopted as multimodal theranostic agents, which is feasible for PA-guided PTT and controlled drug delivery, making them ideal candidates for a smart and multifunctional theranostic platform.

5. Conclusions and Perspectives

PA imaging has emerged as a premier preclinical biomedical imaging technique with various potential configurations. Moreover, many studies have investigated the clinical translation of PA techniques. Although there are limitations in respect to clinical translation at this time, PA imaging may be advantageous for diagnosing diseases and monitoring therapeutic prognoses. As a potential clinical monitoring system, PA images have been used for monitoring phototherapy prognoses using the delivery of 2D nanomaterials that have strong optical absorption properties. To achieve a strong optical contrast in PA images, various structures of 2D nanomaterials have been investigated and showed high optical contrast in PA images as well as a promising therapeutic effects. For future clinical translation and commercialization, 2D nanomaterials should meet requirements such as low toxicity, effective clearance, and high biodegradability. In addition, PA imaging systems need to be improved to achieve a higher signal-to-noise ratio in deep tissue. Because a laser source with a tunable wavelength is costly, 2D nanomaterials that absorb

the 1064 nm wavelength (the default wavelength of Nd:YAG laser) would be a good option for successful commercialization through reducing the system cost.

Author Contributions: W.Y.J., M.S.K. and J.H.L. reviewed and summarized articles, prepared figures, and wrote the manuscript for the part on 2D nanomaterials. H.L. summarized articles and prepared figures for reviewing photoacoustic imaging systems. J.K., D.-W.H., and K.S.K. conceived the structure of the paper, supervised the review, organized the figures, and wrote the manuscript. All authors contributed to the critical reading and writing of the manuscript. All authors have read and agreed to the published version of the manuscript.

Funding: This research was supported by a grant from the Korea Health Technology R&D Project through KHIDI (HI18C2383), funded by the Ministry of Health & Welfare, Republic of Korea and National Research Foundation of Korea (NRF) grant funded by the Korean government (MSIT) (No. 2019R1A4A1024116).

Institutional Review Board Statement: Not applicable.

Informed Consent Statement: Not applicable.

Data Availability Statement: No new data were created or analyzed in this study. Data sharing is not applicable to this article.

Conflicts of Interest: The authors declare no conflict of interest.

References

1. Cao, X.; Halder, A.; Tang, Y.; Hou, C.; Wang, H.; Duus, J.Ø.; Chi, Q. Engineering two-dimensional layered nanomaterials for wearable biomedical sensors and power devices. *Mater. Chem. Front.* **2018**, *2*, 1944–1986. [CrossRef]
2. Hu, T.; Mei, X.; Wang, Y.; Weng, X.; Liang, R.; Wei, M. Two-dimensional nanomaterials: Fascinating materials in biomedical field. *Sci. Bull.* **2019**, *64*, 1707–1727. [CrossRef]
3. Guan, G.; Han, M.Y. Functionalized Hybridization of 2D Nanomaterials. *Adv. Sci.* **2019**, *6*, 1901837. [CrossRef] [PubMed]
4. Yang, F.; Song, P.; Ruan, M.; Xu, W. Recent progress in two-dimensional nanomaterials: Synthesis, engineering, and applications. *FlatChem* **2019**, *18*, 100133. [CrossRef]
5. Fusco, L.; Gazzi, A.; Peng, G.; Shin, Y.; Vranic, S.; Bedognetti, D.; Vitale, F.; Yilmazer, A.; Feng, X.; Fadeel, B. Graphene and other 2D materials: A multidisciplinary analysis to uncover the hidden potential as cancer theranostics. *Theranostics* **2020**, *10*, 5435. [CrossRef]
6. Chimene, D.; Alge, D.L.; Gaharwar, A.K. Two-dimensional nanomaterials for biomedical applications: Emerging trends and future prospects. *Adv. Mater.* **2015**, *27*, 7261–7284. [CrossRef] [PubMed]
7. Sundaram, P.; Abrahamse, H. Phototherapy Combined with Carbon Nanomaterials (1D and 2D) and their Applications in Cancer Therapy. *Mater. Chem. Front.* **2020**, *13*, 4830.
8. Lin, C.; Hao, H.; Mei, L.; Wu, M. Metal-free two-dimensional nanomaterial-mediated photothermal tumor therapy. *Smart Mater. Med.* **2020**, *1*, 150–167. [CrossRef]
9. Liu, S.; Pan, X.; Liu, H. Two-Dimensional Nanomaterials for Photothermal Therapy. *Angew. Chem.* **2020**, *132*, 5943–5953. [CrossRef]
10. Gazzi, A.; Fusco, L.; Khan, A.; Bedognetti, D.; Zavan, B.; Vitale, F.; Yilmazer, A.; Delogu, L.G. Photodynamic therapy based on graphene and MXene in cancer theranostics. *Front. Bioeng. Biotechnol.* **2019**, *7*, 295. [CrossRef]
11. Ritman, E.L. Current status of developments and applications of micro-CT. *Annu. Rev. Biomed. Eng.* **2011**, *13*, 531–552. [CrossRef] [PubMed]
12. Judenhofer, M.S.; Cherry, S.R. Applications for preclinical PET/MRI. In *Seminars in Nuclear Medicine*; Elsevier: Amsterdam, The Netherlands, 2013.
13. Xie, T.; Zaidi, H. Development of computational small animal models and their applications in preclinical imaging and therapy research. *Med. Phys.* **2016**, *43*, 111–131. [CrossRef] [PubMed]
14. Wehrl, H.F.; Wiehr, S.; Divine, M.R.; Gatidis, S.; Gullberg, G.T.; Maier, F.C.; Rolle, A.-M.; Schwenck, J.; Thaiss, W.M.; Pichler, B.J. Preclinical and translational PET/MR imaging. *J. Nucl. Med.* **2014**, *55*, 11S–18S. [CrossRef] [PubMed]
15. Pirovano, G.; Roberts, S.; Kossatz, S.; Reiner, T. Optical imaging modalities: Principles and applications in preclinical research and clinical settings. *J. Nucl. Med.* **2020**, *61*, 1419–1427. [CrossRef]
16. Grashin, P.S.; Karabutov, A.A.; Oraevsky, A.A.; Pelivanov, I.M.; Podymova, N.B.; Savateeva, E.V.; Solomatin, V.S. Distribution of the laser radiation intensity in turbid media: Monte Carlo simulations, theoretical analysis, and results of optoacoustic measurements. *Quantum Electron.* **2002**, *32*, 868. [CrossRef]
17. Bell, A.G. The photophone. *Science* **1880**, *1*, 130–131. [CrossRef]
18. Kim, C.; Favazza, C.; Wang, L.V. In Vivo Photoacoustic Tomography of Chemicals: High-Resolution Functional and Molecular Optical Imaging at New Depths. *Chem. Rev.* **2010**, *110*, 2756–2782. [CrossRef]
19. Kim, J.; Lee, D.; Jung, U.; Kim, C. Photoacoustic imaging platforms for multimodal imaging. *Ultrasonography* **2015**, *34*, 88. [CrossRef]

20. Kim, J.; Park, S.; Lee, C.; Kim, J.Y.; Kim, C. Organic Nanostructures for Photoacoustic Imaging. *ChemNanoMat* **2015**, *2*, 156–166. [CrossRef]
21. Lee, C.; Kim, J.; Zhang, Y.; Jeon, M.; Liu, C.; Song, L.; Lovell, J.F.; Kim, C. Dual-color photoacoustic lymph node imaging using nanoformulated naphthalocyanines. *Biomaterials* **2015**, *73*, 142–148. [CrossRef]
22. Jeon, M.; Song, W.; Huynh, E.; Kim, J.; Kim, J.; Helfield, B.L.; Leung, B.Y.; Goertz, D.E.; Zheng, G.; Oh, J. Methylene blue microbubbles as a model dual-modality contrast agent for ultrasound and activatable photoacoustic imaging. *J. Biomed. Opt.* **2014**, *19*, 016005. [CrossRef] [PubMed]
23. Park, S.; Kim, J.; Jeon, M.; Song, J.; Kim, C. In Vivo Photoacoustic and Fluorescence Cystography Using Clinically Relevant Dual Modal Indocyanine Green. *Sensors* **2014**, *14*, 19660–19668. [CrossRef] [PubMed]
24. Lee, M.Y.; Lee, C.; Jung, H.S.; Jeon, M.; Kim, K.S.; Yun, S.H.; Kim, C.; Hahn, S.K. Biodegradable Photonic Melanoidin for Theranostic Applications. *ACS Nano* **2015**, *10*, 822–831. [CrossRef] [PubMed]
25. De La Zerda, A.; Zavaleta, C.; Keren, S.; Vaithilingam, S.; Bodapati, S.; Liu, Z.; Levi, J.; Smith, B.R.; Ma, T.-J.; Oralkan, O. Carbon nanotubes as photoacoustic molecular imaging agents in living mice. *Nat. Nanotechnol.* **2008**, *3*, 557–562. [CrossRef] [PubMed]
26. Zhang, Y.; Jeon, M.; Rich, L.J.; Hong, H.; Geng, J.; Zhang, Y.; Shi, S.; Barnhart, T.E.; Alexandridis, P.; Huizinga, J.D. Non-Invasive Multimodal Functional Imaging of the Intestine with Frozen Micellar Naphthalocyanines. *Nat. Nanotechnol.* **2014**, *9*, 631–638. [CrossRef]
27. Kim, J.; Park, S.; Jung, Y.; Chang, S.; Park, J.; Zhang, Y.; Lovell, J.F.; Kim, C. Programmable Real-time Clinical Photoacoustic and Ultrasound Imaging System. *Sci. Rep.* **2016**, *6*, 35137. [CrossRef]
28. Jeon, S.; Park, E.-Y.; Choi, W.; Managuli, R.; jong Lee, K.; Kim, C. Real-time delay-multiply-and-sum beamforming with coherence factor for in vivo clinical photoacoustic imaging of humans. *Photoacoustics* **2019**, *15*, 100136. [CrossRef]
29. Park, J.; Jeon, S.; Meng, J.; Song, L.; Lee, J.S.; Kim, C. Delay-multiply-and-sum-based synthetic aperture focusing in photoacoustic microscopy. *J. Biomed. Opt.* **2016**, *21*, 036010. [CrossRef]
30. Yapici, M.K.; Kim, C.; Chang, C.-C.; Jeon, M.; Guo, Z.; Cai, X.; Zou, J.; Wang, L.V. Parallel acoustic delay lines for photoacoustic tomography. *J. Biomed. Opt.* **2012**, *17*, 116019. [CrossRef]
31. Hu, S.; Maslov, K.; Wang, L.V. Second-generation optical-resolution photoacoustic microscopy with improved sensitivity and speed. *Opt. Lett.* **2011**, *36*, 1134–1136. [CrossRef]
32. Bi, R.; Dinish, U.; Goh, C.C.; Imai, T.; Moothanchery, M.; Li, X.; Kim, J.Y.; Jeon, S.; Pu, Y.; Kim, C.; et al. In vivo label-free functional photoacoustic monitoring of ischemic reperfusion. *J. Biophotonics* **2019**, *12*, e201800454. [CrossRef] [PubMed]
33. Yao, J.; Wang, L.V. Photoacoustic Microscopy. *Laser Photonics Rev.* **2013**, *7*, 758–778. [CrossRef] [PubMed]
34. Kim, J.Y.; Lee, C.; Park, K.; Lim, G.; Kim, C. Fast optical-resolution photoacoustic microscopy using a 2-axis water-proofing MEMS scanner. *Sci. Rep.* **2015**, *5*, srep07932. [CrossRef] [PubMed]
35. Ning, B.; Sun, N.; Cao, R.; Chen, R.; Shung, K.K.; Hossack, J.A.; Lee, J.-M.; Zhou, Q.; Hu, S. Ultrasound-aided multi-parametric photoacoustic microscopy of the mouse brain. *Sci. Rep.* **2015**, *5*, 18775. [CrossRef]
36. Lee, D.; Beack, S.; Yoo, J.; Kim, S.K.; Lee, C.; Kwon, W.; Hahn, S.K.; Kim, C. In Vivo Photoacoustic Imaging of Livers Using Biodegradable Hyaluronic Acid-Conjugated Silica Nanoparticles. *Adv. Funct. Mater.* **2018**, *28*, 1800941. [CrossRef]
37. Jung, H.; Park, S.; Gunassekaran, G.R.; Jeon, M.; Cho, Y.-E.; Baek, M.-C.; Park, J.Y.; Shim, G.; Oh, Y.-K.; Kim, I.-S.; et al. A Peptide Probe Enables Pphotoacoustic-Guided Imaging and Drug Delivery to Lung Tumors in K-rasLA2 Mutant Mice. *Cancer Res.* **2019**, *79*, 4271–4282. [CrossRef]
38. Noh, I.; Kim, M.; Kim, J.; Lee, D.; Oh, D.; Kim, J.; Kim, C.; Jon, S.; Kim, Y.-C. Structure-inherent near-infrared bilayer nanovesicles for use as photoacoustic image-guided chemo-thermotherapy. *J. Control. Release* **2020**, *320*, 283–292. [CrossRef]
39. Jeon, M.; Kim, J.; Kim, C. Multiplane spectroscopic whole-body photoacoustic imaging of small animals in vivo. *Med. Biol. Eng. Comput.* **2014**, *54*, 1–12. [CrossRef]
40. Moothanchery, M.; Pramanik, M. Performance characterization of a switchable acoustic resolution and optical resolution photoacoustic microscopy system. *Sensors* **2017**, *17*, 357. [CrossRef]
41. Baik, J.W.; Kim, J.Y.; Cho, S.; Choi, S.; Kim, J.; Kim, C. Super Wide-field Photoacoustic Microscopy of Animals and Humans In Vivo. *IEEE Trans. Med. Imaging* **2019**, *39*, 975–984. [CrossRef]
42. Lin, L.; Xia, J.; Wong, T.T.; Li, L.; Wang, L.V. In vivo deep brain imaging of rats using oral-cavity illuminated photoacoustic computed tomography. *J. Biomed. Opt.* **2015**, *20*, 016019. [CrossRef] [PubMed]
43. Chatni, M.R.; Xia, J.; Sohn, R.; Maslov, K.; Guo, Z.; Zhang, Y.; Wang, K.; Xia, Y.; Anastasio, M.; Arbeit, J.; et al. Tumor glucose metabolism imaged in vivo in small animals with whole-body photoacoustic computed tomography. *J. Biomed. Opt.* **2012**, *17*, 076012. [CrossRef] [PubMed]
44. Wang, D.; Wang, Y.; Wang, W.; Luo, D.; Chitgupi, U.; Geng, J.; Zhou, Y.; Wang, L.; Lovell, J.F.; Xia, J. Deep tissue photoacoustic computed tomography with a fast and compact laser system. *Biomed. Opt. Express* **2017**, *8*, 112–123. [CrossRef] [PubMed]
45. Li, L.; Zhu, L.; Ma, C.; Lin, L.; Yao, J.; Wang, L.; Maslov, K.; Zhang, R.; Chen, W.; Shi, J. Single-impulse panoramic photoacoustic computed tomography of small-animal whole-body dynamics at high spatiotemporal resolution. *Nat. Biomed. Eng.* **2017**, *1*, 1–11. [CrossRef]
46. Heijblom, M.; Steenbergen, W.; Manohar, S. Clinical Photoacoustic Breast Imaging: The Twente experience. *Pulse IEEE* **2015**, *6*, 42–46. [CrossRef]

47. Luís Deán-Ben, X.; Razansky, D. Adding fifth dimension to optoacoustic imaging: Volumetric time-resolved spectrally enriched tomography. *Light Sci. Appl.* **2014**, *3*, e137. [CrossRef]
48. Park, S.; Park, G.; Kim, J.; Choi, W.; Jeong, U.; Kim, C. Bi_2Se_3 nanoplates for contrast-enhanced photoacoustic imaging at 1064 nm. *Nanoscale* **2018**, *10*, 20548–20558. [CrossRef]
49. Chitgupi, U.; Nyayapathi, N.; Kim, J.; Wang, D.; Sun, B.; Li, C.; Carter, K.; Huang, W.C.; Kim, C.; Xia, J. Surfactant-Stripped Micelles for NIR-II Photoacoustic Imaging through 12 cm of Breast Tissue and Whole Human Breasts. *Adv. Mater.* **2019**, *31*, 1902279. [CrossRef]
50. Choi, W.; Park, E.-Y.; Jeon, S.; Kim, C. Clinical photoacoustic imaging platforms. *Biomed. Eng. Lett.* **2018**, *8*, 139–155. [CrossRef]
51. Kim, C.; Erpelding, T.N.; Jankovic, L.; Wang, L.V. Performance benchmarks of an array-based hand-held photoacoustic probe adapted from a clinical ultrasound system for non-invasive sentinel lymph node imaging. *Philos. Trans. R. Soc. A Math. Phys. Eng. Sci.* **2011**, *369*, 4644–4650. [CrossRef]
52. Park, B.; Lee, K.M.; Park, S.; Yun, M.; Choi, H.-J.; Kim, J.; Lee, C.; Kim, H.; Kim, C. Deep tissue photoacoustic imaging of nickel (II) dithiolene-containing polymeric nanoparticles in the second near-infrared window. *Theranostics* **2020**, *10*, 2509. [CrossRef] [PubMed]
53. Toi, M.; Asao, Y.; Matsumoto, Y.; Sekiguchi, H.; Yoshikawa, A.; Takada, M.; Kataoka, M.; Endo, T.; Kawaguchi-Sakita, N.; Kawashima, M. Visualization of tumor-related blood vessels in human breast by photoacoustic imaging system with a hemispherical detector array. *Sci. Rep.* **2017**, *7*, 41970. [CrossRef] [PubMed]
54. Kim, J.; Kim, Y.H.; Park, B.; Seo, H.M.; Bang, C.H.; Park, G.S.; Park, Y.M.; Rhie, J.W.; Lee, J.H.; Kim, C. Multispectral *Ex Vivo* Photoacoustic Imaging of Cutaneous Melanoma for Better Selection of the Excision Margin. *Br. J. Dermatol.* **2018**, *179*, 780–782. [CrossRef] [PubMed]
55. Neuschler, E.I.; Butler, R.; Young, C.A.; Barke, L.D.; Bertrand, M.L.; Böhm-Vélez, M.; Destounis, S.; Donlan, P.; Grobmyer, S.R.; Katzen, J. A pivotal study of optoacoustic imaging to diagnose benign and malignant breast masses: A new evaluation tool for radiologists. *Radiology* **2017**, *287*, 398–412. [CrossRef] [PubMed]
56. Aguirre, J.; Schwarz, M.; Garzorz, N.; Omar, M.; Buehler, A.; Eyerich, K.; Ntziachristos, V. Precision assessment of label-free psoriasis biomarkers with ultra-broadband optoacoustic mesoscopy. *Nat. Biomed. Eng.* **2017**, *1*, 1–8. [CrossRef]
57. Lin, J.; Huang, Y.; Huang, P. Graphene-based nanomaterials in bioimaging. In *Biomedical Applications of Functionalized Nanomaterials*; Elsevier: Amsterdam, The Netherlands, 2018; pp. 247–287.
58. Tang, Y.; Zhao, Z.; Hu, H.; Liu, Y.; Wang, X.; Zhou, S.; Qiu, J. Highly stretchable and ultrasensitive strain sensor based on reduced graphene oxide microtubes–elastomer composite. *ACS Appl. Mater. Interfaces* **2015**, *7*, 27432–27439. [CrossRef]
59. Savchuk, O.A.; Carvajal, J.; Massons, J.; Aguiló, M.; Díaz, F. Determination of photothermal conversion efficiency of graphene and graphene oxide through an integrating sphere method. *Carbon* **2016**, *103*, 134–141. [CrossRef]
60. Zhu, X.; Liu, Y.; Li, P.; Nie, Z.; Li, J. Applications of graphene and its derivatives in intracellular biosensing and bioimaging. *Analyst* **2016**, *141*, 4541–4553. [CrossRef]
61. Wang, Y.; Wang, H.; Liu, D.; Song, S.; Wang, X.; Zhang, H. Graphene oxide covalently grafted upconversion nanoparticles for combined NIR mediated imaging and photothermal/photodynamic cancer therapy. *Biomaterials* **2013**, *34*, 7715–7724. [CrossRef]
62. Yang, Y.; Shi, H.; Wang, Y.; Shi, B.; Guo, L.; Wu, D.; Yang, S.; Wu, H. Graphene oxide/manganese ferrite nanohybrids for magnetic resonance imaging, photothermal therapy and drug delivery. *J. Biomater. Appl.* **2016**, *30*, 810–822. [CrossRef]
63. Rives, V.; del Arco, M.; Martín, C. Intercalation of drugs in layered double hydroxides and their controlled release: A review. *Appl. Clay Sci.* **2014**, *88*, 239–269. [CrossRef]
64. Khan, S.B.; Alamry, K.A.; Alyahyawi, N.A.; Asiri, A.M.; Arshad, M.N.; Marwani, H.M. Nanohybrid based on antibiotic encapsulated layered double hydroxide as a drug delivery system. *Appl. Biochem. Biotechnol.* **2015**, *175*, 1412–1428. [CrossRef] [PubMed]
65. Bi, X.; Fan, T.; Zhang, H. Novel morphology-controlled hierarchical core@ shell structural organo-layered double hydroxides magnetic nanovehicles for drug release. *ACS Appl. Mater. Interfaces* **2014**, *6*, 20498–20509. [CrossRef] [PubMed]
66. Liu, P.; Xiang, B. 2D hetero-structures based on transition metal dichalcogenides: Fabrication, properties and applications. *Sci. Bull.* **2017**, *62*, 1148–1161. [CrossRef]
67. Fu, C.; Tan, L.; Ren, X.; Wu, Q.; Shao, H.; Ren, J.; Zhao, Y.; Meng, X. Interlayer expansion of 2D MoS_2 nanosheets for highly improved photothermal therapy of tumors in vitro and in vivo. *Chem. Commun.* **2018**, *54*, 13989–13992. [CrossRef]
68. Cui, X.-Z.; Zhou, Z.-G.; Yang, Y.; Wei, J.; Wang, J.; Wang, M.-W.; Yang, H.; Zhang, Y.-J.; Yang, S.-P. PEGylated WS2 nanosheets for X-ray computed tomography imaging and photothermal therapy. *Chin. Chem. Lett.* **2015**, *26*, 749–754. [CrossRef]
69. He, L.; Nie, T.; Xia, X.; Liu, T.; Huang, Y.; Wang, X.; Chen, T. Designing Bioinspired 2D $MoSe_2$ Nanosheet for Efficient Photothermal-Triggered Cancer Immunotherapy with Reprogramming Tumor-Associated Macrophages. *Adv. Funct. Mater.* **2019**, *29*, 1901240. [CrossRef]
70. Pumera, M.; Loo, A.H. Layered transition-metal dichalcogenides (MoS_2 and WS_2) for sensing and biosensing. *Trac Trends Anal. Chem.* **2014**, *61*, 49–53. [CrossRef]
71. Liu, J.; Zheng, J.; Nie, H.; Zhang, D.; Cao, D.; Xing, Z.; Li, B.; Jia, L. Molybdenum disulfide-based hyaluronic acid-guided multifunctional theranostic nanoplatform for magnetic resonance imaging and synergetic chemo-photothermal therapy. *J. Colloid Interface Sci.* **2019**, *548*, 131–144. [CrossRef]

72. Maji, S.K.; Yu, S.; Chung, K.; Sekkarapatti Ramasamy, M.; Lim, J.W.; Wang, J.; Lee, H.; Kim, D.H. Synergistic Nanozymetic Activity of Hybrid Gold Bipyramid–Molybdenum Disulfide Core@ Shell Nanostructures for Two-Photon Imaging and Anticancer Therapy. *ACS Appl. Mater. Interfaces* **2018**, *10*, 42068–42076. [CrossRef]
73. Chen, L.; Zhou, X.; Nie, W.; Feng, W.; Zhang, Q.; Wang, W.; Zhang, Y.; Chen, Z.; Huang, P.; He, C. Marriage of Albumin–Gadolinium Complexes and MoS_2 Nanoflakes as Cancer Theranostics for Dual-Modality Magnetic Resonance/Photoacoustic Imaging and Photothermal Therapy. *ACS Appl. Mater. Interfaces* **2017**, *9*, 17786–17798. [CrossRef] [PubMed]
74. Chia, X.; Eng, A.Y.S.; Ambrosi, A.; Tan, S.M.; Pumera, M. Electrochemistry of nanostructured layered transition-metal dichalcogenides. *Chem. Rev.* **2015**, *115*, 11941–11966. [CrossRef] [PubMed]
75. Yong, Y.; Zhou, L.; Gu, Z.; Yan, L.; Tian, G.; Zheng, X.; Liu, X.; Zhang, X.; Shi, J.; Cong, W. WS_2 nanosheet as a new photosensitizer carrier for combined photodynamic and photothermal therapy of cancer cells. *Nanoscale* **2014**, *6*, 10394–10403. [CrossRef] [PubMed]
76. Cheng, L.; Liu, J.; Gu, X.; Gong, H.; Shi, X.; Liu, T.; Wang, C.; Wang, X.; Liu, G.; Xing, H. PEGylated WS_2 nanosheets as a multifunctional theranostic agent for in vivo dual-modal CT/photoacoustic imaging guided photothermal therapy. *Adv. Mater.* **2014**, *26*, 1886–1893. [CrossRef]
77. Yang, G.; Zhang, R.; Liang, C.; Zhao, H.; Yi, X.; Shen, S.; Yang, K.; Cheng, L.; Liu, Z. Manganese Dioxide Coated WS2@ Fe_3O_4/$sSiO_2$ Nanocomposites for pH-Responsive MR Imaging and Oxygen-Elevated Synergetic Therapy. *Small* **2018**, *14*, 1702664. [CrossRef]
78. Zhou, X.; Sun, H.; Bai, X. Two-Dimensional Transition Metal Dichalcogenides: Synthesis, Biomedical Applications and Biosafety Evaluation. *Front. Bioeng. Biotechnol.* **2020**, *8*, 8. [CrossRef]
79. Wang, Y.; Zhang, F.; Lin, H.; Qu, F. Biodegradable Hollow $MoSe_2$/Fe_3O_4 Nanospheres as the Photodynamic Therapy-Enhanced Agent for Multimode CT/MR/IR Imaging and Synergistic Antitumor Therapy. *ACS Appl. Mater. Interfaces* **2019**, *11*, 43964–43975. [CrossRef]
80. Wang, Y.; Zhang, F.; Wang, Q.; Yang, P.; Lin, H.; Qu, F. Hierarchical $MoSe_2$ nanoflowers as novel nanocarriers for NIR-light-mediated synergistic photo-thermal/dynamic and chemo-therapy. *Nanoscale* **2018**, *10*, 14534–14545. [CrossRef]
81. Moosavi, M.A.; Sharifi, M.; Ghafary, S.M.; Mohammadalipour, Z.; Khataee, A.; Rahmati, M.; Hajjaran, S.; Łos, M.J.; Klonisch, T.; Ghavami, S. Photodynamic N-TiO 2 nanoparticle treatment induces controlled ROS-mediated autophagy and terminal differentiation of leukemia cells. *Sci. Rep.* **2016**, *6*, 1–16. [CrossRef]
82. Nie, C.; Du, P.; Zhao, H.; Xie, H.; Li, Y.; Yao, L.; Shi, Y.; Hu, L.; Si, S.; Zhang, M. Ag@ TiO_2 Nanoprisms with Highly Efficient Near-Infrared Photothermal Conversion for Melanoma Therapy. *Chem. Asian J.* **2020**, *15*, 148–155. [CrossRef]
83. Chen, Y.; Ye, D.; Wu, M.; Chen, H.; Zhang, L.; Shi, J.; Wang, L. Break-up of Two-Dimensional MnO_2 Nanosheets Promotes Ultrasensitive pH-Triggered Theranostics of Cancer. *Adv. Mater.* **2014**, *26*, 7019–7026. [CrossRef] [PubMed]
84. Hao, Y.; Wang, L.; Zhang, B.; Zhao, H.; Niu, M.; Hu, Y.; Zheng, C.; Zhang, H.; Chang, J.; Zhang, Z. Multifunctional nanosheets based on folic acid modified manganese oxide for tumor-targeting theranostic application. *Nanotechnology* **2015**, *27*, 025101. [CrossRef] [PubMed]
85. Wang, Y.; Song, Y.; Zhu, G.; Zhang, D.; Liu, X. Highly biocompatible BSA-MnO_2 nanoparticles as an efficient near-infrared photothermal agent for cancer therapy. *Chin. Chem. Lett.* **2018**, *29*, 1685–1688. [CrossRef]
86. Li, W.; Elzatahry, A.; Aldhayan, D.; Zhao, D. Core–shell structured titanium dioxide nanomaterials for solar energy utilization. *Chem. Soc. Rev.* **2018**, *47*, 8203–8237. [CrossRef] [PubMed]
87. Wang, L.; Guan, S.; Weng, Y.; Xu, S.-M.; Lu, H.; Meng, X.; Zhou, S. Highly efficient vacancy-driven photothermal therapy mediated by ultrathin MnO2 nanosheets. *ACS Appl. Mater. Interfaces* **2019**, *11*, 6267–6275. [CrossRef]
88. Ma, R.; Sasaki, T. Nanosheets of oxides and hydroxides: Ultimate 2D charge-bearing functional crystallites. *Adv. Mater.* **2010**, *22*, 5082–5104. [CrossRef] [PubMed]
89. Kalantar-zadeh, K.; Ou, J.Z.; Daeneke, T.; Mitchell, A.; Sasaki, T.; Fuhrer, M.S. Two dimensional and layered transition metal oxides. *Appl. Mater. Today* **2016**, *5*, 73–89. [CrossRef]
90. Azadmanjiri, J.; Kumar, P.; Srivastava, V.K.; Sofer, Z. Surface Functionalization of 2D Transition Metal Oxides and Dichalcogenides via Covalent and Non-covalent Bonding for Sustainable Energy and Biomedical Applications. *ACS Appl. Nano Mater.* **2020**, *3*, 3116–3143. [CrossRef]
91. Lin, H.; Wang, X.; Yu, L.; Chen, Y.; Shi, J. Two-dimensional ultrathin MXene ceramic nanosheets for photothermal conversion. *Nano Lett.* **2017**, *17*, 384–391. [CrossRef]
92. Li, R.; Zhang, L.; Shi, L.; Wang, P. MXene Ti_3C_2: An effective 2D light-to-heat conversion material. *ACS Nano* **2017**, *11*, 3752–3759. [CrossRef]
93. Tang, W.; Dong, Z.; Zhang, R.; Yi, X.; Yang, K.; Jin, M.; Yuan, C.; Xiao, Z.; Liu, Z.; Cheng, L. Multifunctional two-dimensional core–shell mxene@ gold nanocomposites for enhanced photo–radio combined therapy in the second biological window. *ACS Nano* **2018**, *13*, 284–294. [CrossRef] [PubMed]
94. Han, X.; Huang, J.; Lin, H.; Wang, Z.; Li, P.; Chen, Y. 2D ultrathin MXene-based drug-delivery nanoplatform for synergistic photothermal ablation and chemotherapy of cancer. *Adv. Healthc. Mater.* **2018**, *7*, 1701394. [CrossRef] [PubMed]
95. Liu, G.; Zou, J.; Tang, Q.; Yang, X.; Zhang, Y.; Zhang, Q.; Huang, W.; Chen, P.; Shao, J.; Dong, X. Surface modified Ti_3C_2 MXene nanosheets for tumor targeting photothermal/photodynamic/chemo synergistic therapy. *ACS Appl. Mater. Interfaces* **2017**, *9*, 40077–40086. [CrossRef] [PubMed]

96. Choi, J.R.; Yong, K.W.; Choi, J.Y.; Nilghaz, A.; Lin, Y.; Xu, J.; Lu, X. Black phosphorus and its biomedical applications. *Theranostics* **2018**, *8*, 1005. [CrossRef]
97. Xu, D.; Liu, J.; Wang, Y.; Jian, Y.; Wu, W.; Lv, R. Black Phosphorus Nanosheet with High Thermal Conversion Efficiency for Photodynamic/Photothermal/Immunotherapy. *ACS Biomater. Sci. Eng.* **2020**, *6*, 4940–4948. [CrossRef]
98. Yang, G.; Liu, Z.; Li, Y.; Hou, Y.; Fei, X.; Su, C.; Wang, S.; Zhuang, Z.; Guo, Z. Facile synthesis of black phosphorus–Au nanocomposites for enhanced photothermal cancer therapy and surface-enhanced Raman scattering analysis. *Biomater. Sci.* **2017**, *5*, 2048–2055. [CrossRef]
99. Tao, W.; Zhu, X.; Yu, X.; Zeng, X.; Xiao, Q.; Zhang, X.; Ji, X.; Wang, X.; Shi, J.; Zhang, H. Black phosphorus nanosheets as a robust delivery platform for cancer theranostics. *Adv. Mater.* **2017**, *29*, 1603276. [CrossRef]
100. Yang, X.; Wang, D.; Shi, Y.; Zou, J.; Zhao, Q.; Zhang, Q.; Huang, W.; Shao, J.; Xie, X.; Dong, X. Black phosphorus nanosheets immobilizing Ce6 for imaging-guided photothermal/photodynamic cancer therapy. *ACS Appl. Mater. Interfaces* **2018**, *10*, 12431–12440. [CrossRef]
101. Xiong, S.; Chen, X.; Liu, Y.; Fan, T.; Wang, Q.; Zhang, H.; Chen, T. Black phosphorus as a versatile nanoplatform: From unique properties to biomedical applications. *J. Innov. Opt. Health Sci.* **2020**. [CrossRef]
102. Liu, T.; Wang, C.; Gu, X.; Gong, H.; Cheng, L.; Shi, X.; Feng, L.; Sun, B.; Liu, Z. Drug delivery with PEGylated MoS_2 nano-sheets for combined photothermal and chemotherapy of cancer. *Adv. Mater.* **2014**, *26*, 3433–3440. [CrossRef]
103. Zeng, D.; Wang, L.; Tian, L.; Zhao, S.; Zhang, X.; Li, H. Synergistic photothermal/photodynamic suppression of prostatic carcinoma by targeted biodegradable MnO_2 nanosheets. *Drug Deliv.* **2019**, *26*, 661–672. [CrossRef] [PubMed]
104. Ji, X.; Kong, N.; Wang, J.; Li, W.; Xiao, Y.; Gan, S.T.; Zhang, Y.; Li, Y.; Song, X.; Xiong, Q. A novel top-down synthesis of ultrathin 2D boron nanosheets for multimodal imaging-guided cancer therapy. *Adv. Mater.* **2018**, *30*, 1803031. [CrossRef] [PubMed]
105. Kang, Y.; Ji, X.; Li, Z.; Su, Z.; Zhang, S. Boron-based nanosheets for combined cancer photothermal and photodynamic therapy. *J. Mater. Chem. B* **2020**, *8*, 4609–4619. [CrossRef] [PubMed]
106. Yan, L.; Wang, Y.; Hu, T.; Mei, X.; Zhao, X.; Bian, Y.; Jin, L.; Liang, R.; Weng, X.; Wei, M. Layered double hydroxide nanosheets: Towards ultrasensitive tumor microenvironment responsive synergistic therapy. *J. Mater. Chem. B* **2020**, *8*, 1445–1455. [CrossRef] [PubMed]
107. Chen, J.; Liu, C.; Zeng, G.; You, Y.; Wang, H.; Gong, X.; Zheng, R.; Kim, J.; Kim, C.; Song, L. Indocyanine green loaded reduced graphene oxide for in vivo photoacoustic/fluorescence dual-modality tumor imaging. *Nanoscale Res. Lett.* **2016**, *11*, 1–11. [CrossRef] [PubMed]
108. Yu, J.; Wang, X.H.; Feng, J.; Meng, X.; Bu, X.; Li, Y.; Zhang, N.; Wang, P. Antimonene Nanoflakes: Extraordinary Photoacoustic Performance for High-Contrast Imaging of Small Volume Tumors. *Adv. Healthc. Mater.* **2019**, *8*, 1900378. [CrossRef]
109. Zhou, Y.; Feng, W.; Qian, X.; Yu, L.; Han, X.; Fan, G.; Chen, Y.; Zhu, J. Construction of 2D Antimony (III) Selenide Nanosheets for Highly Efficient Photonic Cancer Theranostics. *ACS Appl. Mater. Interfaces* **2019**, *11*, 19712–19723. [CrossRef]
110. Lin, H.; Wang, Y.; Gao, S.; Chen, Y.; Shi, J. Theranostic 2D tantalum carbide (MXene). *Adv. Mater.* **2018**, *30*, 1703284. [CrossRef]
111. Dai, C.; Chen, Y.; Jing, X.; Xiang, L.; Yang, D.; Lin, H.; Liu, Z.; Han, X.; Wu, R. Two-dimensional tantalum carbide (MXenes) composite nanosheets for multiple imaging-guided photothermal tumor ablation. *ACS Nano* **2017**, *11*, 12696–12712. [CrossRef]
112. Xie, H.; Li, Z.; Sun, Z.; Shao, J.; Yu, X.F.; Guo, Z.; Wang, J.; Xiao, Q.; Wang, H.; Wang, Q.Q. Metabolizable ultrathin Bi_2Se_3 nanosheets in imaging-guided photothermal therapy. *Small* **2016**, *12*, 4136–4145. [CrossRef]
113. Xie, H.; Liu, M.; You, B.; Luo, G.; Chen, Y.; Liu, B.; Jiang, Z.; Chu, P.K.; Shao, J.; Yu, X.F. Biodegradable Bi_2O_2Se Quantum Dots for Photoacoustic Imaging-Guided Cancer Photothermal Therapy. *Small* **2020**, *16*, 1905208. [CrossRef] [PubMed]
114. Song, Y.; Wang, J.; Liu, L.; Sun, Q.; You, Q.; Cheng, Y.; Wang, Y.; Wang, S.; Tan, F.; Li, N. One-pot synthesis of a bismuth selenide hexagon nanodish complex for multimodal imaging-guided combined antitumor phototherapy. *Mol. Pharm.* **2018**, *15*, 1941–1953. [CrossRef] [PubMed]
115. Shin, M.H.; Park, E.Y.; Han, S.; Jung, H.S.; Keum, D.H.; Lee, G.H.; Kim, T.; Kim, C.; Kim, K.S.; Yun, S.H. Multimodal cancer theranosis using hyaluronate-conjugated molybdenum disulfide. *Adv. Healthc. Mater.* **2019**, *8*, 1801036. [CrossRef] [PubMed]
116. Liu, T.; Shi, S.; Liang, C.; Shen, S.; Cheng, L.; Wang, C.; Song, X.; Goel, S.; Barnhart, T.E.; Cai, W. Iron oxide decorated MoS_2 nanosheets with double PEGylation for chelator-free radiolabeling and multimodal imaging guided photothermal therapy. *ACS Nano* **2015**, *9*, 950–960. [CrossRef] [PubMed]
117. Wang, S.; Li, X.; Chen, Y.; Cai, X.; Yao, H.; Gao, W.; Zheng, Y.; An, X.; Shi, J.; Chen, H. A facile one-pot synthesis of a two-dimensional MoS2/Bi2S3 composite theranostic nanosystem for multi-modality tumor imaging and therapy. *Adv. Mater.* **2015**, *27*, 2775–2782. [CrossRef] [PubMed]
118. Zhu, W.; Chen, M.; Liu, Y.; Tian, Y.; Song, Z.; Song, G.; Zhang, X. A dual factor activated metal–organic framework hybrid nanoplatform for photoacoustic imaging and synergetic photo-chemotherapy. *Nanoscale* **2019**, *11*, 20630–20637. [CrossRef]
119. Chen, M.; Tang, S.; Guo, Z.; Wang, X.; Mo, S.; Huang, X.; Liu, G.; Zheng, N. Core–Shell Pd@ Au Nanoplates as Theranostic Agents for In-Vivo Photoacoustic Imaging, CT Imaging, and Photothermal Therapy. *Adv. Mater.* **2014**, *26*, 8210–8216. [CrossRef]
120. Xie, Z.; Chen, S.; Duo, Y.; Zhu, Y.; Fan, T.; Zou, Q.; Qu, M.; Lin, Z.; Zhao, J.; Li, Y. Biocompatible two-dimensional titanium nanosheets for multimodal imaging-guided cancer theranostics. *ACS Appl. Mater. Interfaces* **2019**, *11*, 22129–22140. [CrossRef]
121. Ouyang, J.; Feng, C.; Ji, X.; Li, L.; Gutti, H.K.; Kim, N.Y.; Artzi, D.; Xie, A.; Kong, N.; Liu, Y.N. 2D monoelemental germanene quantum dots: Synthesis as robust photothermal agents for photonic cancer nanomedicine. *Angew. Chem.* **2019**, *131*, 13539–13544. [CrossRef]

122. Jin, Z.; Chen, D.; Zhao, P.; Wen, Y.; Fan, M.; Zhou, G.; Wang, Y.; He, Q. Coordination-induced exfoliation to monolayer Bi-anchored MnB2 nanosheets for multimodal imaging-guided photothermal therapy of cancer. *Theranostics* **2020**, *10*, 1861. [CrossRef]
123. Tang, W.; Fan, W.; Zhang, W.; Yang, Z.; Li, L.; Wang, Z.; Chiang, Y.L.; Liu, Y.; Deng, L.; He, L. Wet/sono-chemical synthesis of enzymatic two-dimensional MnO_2 nanosheets for synergistic catalysis-enhanced phototheranostics. *Adv. Mater.* **2019**, *31*, 1900401. [CrossRef] [PubMed]
124. Wang, S.; Zhao, J.; Yang, H.; Wu, C.; Hu, F.; Chang, H.; Li, G.; Ma, D.; Zou, D.; Huang, M. Bottom-up synthesis of WS_2 nanosheets with synchronous surface modification for imaging guided tumor regression. *Acta Biomater.* **2017**, *58*, 442–454. [CrossRef] [PubMed]
125. Song, X.R.; Wang, X.; Yu, S.X.; Cao, J.; Li, S.H.; Li, J.; Liu, G.; Yang, H.H.; Chen, X. Co9Se8 nanoplates as a new theranostic platform for photoacoustic/magnetic resonance Dual-Modal-Imaging-Guided Chemo-Photothermal combination therapy. *Adv. Mater.* **2015**, *27*, 3285–3291. [CrossRef]
126. Liu, Y.; Wang, Z.; Liu, Y.; Zhu, G.; Jacobson, O.; Fu, X.; Bai, R.; Lin, X.; Lu, N.; Yang, X. Suppressing nanoparticle-mononuclear phagocyte system interactions of two-dimensional gold nanorings for improved tumor accumulation and photothermal ablation of tumors. *ACS Nano* **2017**, *11*, 10539–10548. [CrossRef] [PubMed]
127. Ke, K.; Yang, W.; Xie, X.; Liu, R.; Wang, L.-L.; Lin, W.-W.; Huang, G.; Lu, C.-H.; Yang, H.-H. Copper manganese sulfide nanoplates: A new two-dimensional theranostic nanoplatform for MRI/MSOT dual-modal imaging-guided photothermal therapy in the second near-infrared window. *Theranostics* **2017**, *7*, 4763. [CrossRef]
128. Qian, X.; Shen, S.; Liu, T.; Cheng, L.; Liu, Z.J.N. Two-dimensional TiS 2 nanosheets for in vivo photoacoustic imaging and photothermal cancer therapy. *Nanoscale* **2015**, *7*, 6380–6387. [CrossRef]
129. Huang, P.; Lin, J.; Li, W.; Rong, P.; Wang, Z.; Wang, S.; Wang, X.; Sun, X.; Aronova, M.; Niu, G. Biodegradable gold nanovesicles with an ultrastrong plasmonic coupling effect for photoacoustic imaging and photothermal therapy. *Angew. Chem.* **2013**, *125*, 14208–14214. [CrossRef]
130. Lyu, Y.; Fang, Y.; Miao, Q.; Zhen, X.; Ding, D.; Pu, K. Intraparticle molecular orbital engineering of semiconducting polymer nanoparticles as amplified theranostics for in vivo photoacoustic imaging and photothermal therapy. *ACS Nano* **2016**, *10*, 4472–4481. [CrossRef]
131. Ares, P.; Aguilar-Galindo, F.; Rodríguez-San-Miguel, D.; Aldave, D.A.; Díaz-Tendero, S.; Alcamí, M.; Martín, F.; Gómez-Herrero, J.; Zamora, F. Mechanical isolation of highly stable antimonene under ambient conditions. *Adv. Mater.* **2016**, *28*, 6332–6336. [CrossRef]
132. Evans, P.M. Anatomical imaging for radiotherapy. *Phys. Med. Biol.* **2008**, *53*, R151. [CrossRef]
133. Li, Z.; Liang, X.; Li, G.; Liu, H.; Zhang, H.; Guo, J.; Chen, J.; Shen, K.; San, X.; Yu, W. 9.2%-efficient core-shell structured antimony selenide nanorod array solar cells. *Nat. Commun.* **2019**, *10*, 1–9. [CrossRef] [PubMed]
134. Mashtalir, O.; Naguib, M.; Mochalin, V.N.; Dall'Agnese, Y.; Heon, M.; Barsoum, M.W.; Gogotsi, Y. Intercalation and delamination of layered carbides and carbonitrides. *Nat. Commun.* **2013**, *4*, 1–7. [CrossRef] [PubMed]
135. Zhang, H.; Liu, C.-X.; Qi, X.-L.; Dai, X.; Fang, Z.; Zhang, S.-C. Topological insulators in Bi_2Se_3, Bi_2Te_3 and Sb_2Te_3 with a single Dirac cone on the surface. *Nat. Phys.* **2009**, *5*, 438–442. [CrossRef]
136. Wang, M.-X.; Liu, C.; Xu, J.-P.; Yang, F.; Miao, L.; Yao, M.-Y.; Gao, C.; Shen, C.; Ma, X.; Chen, X. The coexistence of superconductivity and topological order in the Bi_2Se_3 thin films. *Science* **2012**, *336*, 52–55. [CrossRef] [PubMed]
137. Peng, H.; Dang, W.; Cao, J.; Chen, Y.; Wu, D.; Zheng, W.; Li, H.; Shen, Z.-X.; Liu, Z. Topological insulator nanostructures for near-infrared transparent flexible electrodes. *Nat. Chem.* **2012**, *4*, 281–286. [CrossRef]
138. Wang, S.; Li, K.; Chen, Y.; Chen, H.; Ma, M.; Feng, J.; Zhao, Q.; Shi, J. Biocompatible PEGylated MoS_2 nanosheets: Controllable bottom-up synthesis and highly efficient photothermal regression of tumor. *Biomaterials* **2015**, *39*, 206–217. [CrossRef]
139. Yin, W.; Yan, L.; Yu, J.; Tian, G.; Zhou, L.; Zheng, X.; Zhang, X.; Yong, Y.; Li, J.; Gu, Z. High-throughput synthesis of single-layer MoS_2 nanosheets as a near-infrared photothermal-triggered drug delivery for effective cancer therapy. *ACS Nano* **2014**, *8*, 6922–6933. [CrossRef]
140. Oh, E.J.; Park, K.; Kim, K.S.; Kim, J.; Yang, J.-A.; Kong, J.-H.; Lee, M.Y.; Hoffman, A.S.; Hahn, S.K. Target specific and long-acting delivery of protein, peptide, and nucleotide therapeutics using hyaluronic acid derivatives. *J. Control. Release* **2010**, *141*, 2–12. [CrossRef]
141. Johnson, L.A.; Banerji, S.; Lawrance, W.; Gileadi, U.; Prota, G.; Holder, K.A.; Roshorm, Y.M.; Hanke, T.; Cerundolo, V.; Gale, N.W. Dendritic cells enter lymph vessels by hyaluronan-mediated docking to the endothelial receptor LYVE-1. *Nat. Immunol.* **2017**, *18*, 762. [CrossRef]
142. Guo, Z.; Chen, M.; Peng, C.; Mo, S.; Shi, C.; Fu, G.; Wen, X.; Zhuang, R.; Su, X.; Liu, T. pH-sensitive radiolabeled and superfluorinated ultra-small palladium nanosheet as a high-performance multimodal platform for tumor theranostics. *Biomaterials* **2018**, *179*, 134–143. [CrossRef]
143. Syverud, M.; Dahl, J.; Herø, H.; Morisbak, E. Corrosion and biocompatibility testing of palladium alloy castings. *Dent. Mater.* **2001**, *17*, 7–13. [CrossRef]
144. Tang, S.; Chen, M.; Zheng, N. Multifunctional ultrasmall Pd nanosheets for enhanced near-infrared photothermal therapy and chemotherapy of cancer. *Nano Res.* **2015**, *8*, 165–174. [CrossRef]